

Observation of Sea Ice Surface Thermal States under Cloud Cover

S. V. Nghiem¹, D. K. Perovich², A. J. Gow², R. Kwok¹,
D. G. Barber³, and J. C. Comiso⁴

¹Jet Propulsion Laboratory
California Institute of Technology
Pasadena, California, USA

² U.S. Army Cold Regions Research
and Engineering Laboratory
Hanover, New Hampshire, USA

³ Department of Geography
University of Manitoba
Winnipeg, Manitoba, Canada

⁴ National Aeronautics and Space Administration
Goddard Space Flight Center
Greenbelt, Maryland, USA

Observation of Sea Ice Surface Thermal States under Cloud Cover

S. V. Nghiem¹, D. K. Perovich², A. J. Gow², R. Kwok¹,

D. G. Barber³, and J. C. Comiso⁴

¹*Center for Space Microelectronics Technology*

Jet Propulsion Laboratory, California Institute of Technology

Pasadena, California 91109, U.S.A.

²*U.S. Army Cold Regions Research and Engineering Laboratory*

Hanover, New Hampshire 03755

³*Department of Geography, University of Manitoba*

Winnipeg, Manitoba R3T 2N2, Canada

⁴*Goddard Space Flight Center, Code 971*

Greenbelt, Maryland 20771, U.S.A.

Abstract – Clouds interfere with the distribution of short-wave and long-wave radiations over sea ice, and thereby strongly affect the surface energy balance in polar regions. To evaluate the overall effects of clouds on climatic feedback processes in the atmosphere-ice-ocean system, the challenge is to observe sea ice surface thermal states under both clear sky and cloudy conditions. From laboratory experiments, we show that C-band radar (transparent to clouds) backscatter is very sensitive to surface temperature of first-year sea ice. The effect of sea ice surface temperature on the magnitude of backscatter change depends on the thermal regimes of sea ice thermodynamic states. For the temperature range above

the mirabilite ($\text{Na}_2\text{SO}_4 \cdot 10\text{H}_2\text{O}$) crystallization point (-8.2°C), C-band data show sea ice backscatter changes by 8-10 dB for incident angles from 20° to 35° at both horizontal and vertical polarizations. For temperatures below the mirabilite point but above the crystallization point of $\text{MgCl}_2 \cdot 8\text{H}_2\text{O}$ (-18.0°C), relatively strong backscatter changes between 4-6 dB are observed. These backscatter changes correspond to approximately 8°C change in temperature for both cases. The backscattering mechanism is related to the temperature, which determines the thermodynamic distribution of brine volume in the sea ice surface layer. The backscatter is positively correlated to temperature and the process is reversible with thermodynamic variations such as diurnal insolation effects. From two different dates in May 1993 with clear and overcast conditions determined by the Advanced Very High Resolution Radiometer (AVHRR), concurrent Earth Resources Satellite 1 (ERS-1) C-band Synthetic Aperture Radar (SAR) data show the warming 'blanket effect' of clouds on sea ice observed with increases in backscatter over first-year sea ice, and verified by increases in in-situ sea ice surface temperatures measured at the Collaborative-Interdisciplinary Cryosphere Experiment (C-ICE) site.

I. INTRODUCTION

1. Background

The formation, evolution, and decay of snow-covered sea ice throughout annual cycles induce dramatic changes in the interactions between ocean and atmosphere and exert a significant influence on global climate patterns. Changes in sea ice surface thermal states lead to modifications of surface albedo, which cause further changes in surface heat balance and subsequently changes in ice surface temperature. An amplification effect in the ice-albedo feedback process has been long recognized [*Croll*, 1875]. Various simulations of

global warming have indicated the importance the ice-albedo feedback [Ingram *et al.*, 1989, Rind *et al.*, 1995]. Manabe *et al.* [1991] has simulated a centennial carbon dioxide increase scenario, which indicates a poleward amplification of surface temperature change.

In the feedback process, cloud cover interferes with the distribution of short-wave and long-wave radiations, and thus strongly affects the surface energy balance [Ambach, 1974, Curry and Ebert, 1992, Barber and Thomas, 1998, Barber *et al.*, 1998]. In the seasonal cycle, effects of clouds are particularly important during the late spring and summer when the mean cloudiness is high and the insolation is strong [Moritz and Perovich, 1996]. A large increase in cloudiness over sea ice during a strong insolation period may damp the positive ice-albedo feedback effect, whereas a decrease in cloudiness may further amplify the ice-albedo feedback [Moritz and Perovich, 1996].

2. Scientific Issues

Polar cloud feedback mechanisms in the atmosphere-ice-ocean system are complicated and it is not certain whether the net feedback process is positive or negative [Moritz *et al.*, 1993]. A positive cloud effect has been estimated in the Arctic [Curry *et al.*, 1996] while a negative cloud feedback has been estimated globally [Cess *et al.*, 1989]. Kellogg [1973] discusses another point of view stating that the albedo cloud cover temperature loop is negative in polar regions and positive away from the poles. The speculative Simpson hypothesis suggests that increasing insolation leads to an integral decrease in polar region temperature through a chain of interrelated phenomena involving increasing solar radiation, evaporation, cloudiness, and snow precipitation [Antonov and 50 others in Russian Academy of Sciences, 1995]. The uncertainties result in large discrepancies in the Arctic and global climate simulated by different General Circulation Models (GCM) [Moritz *et al.*, 1993].

Depending on geographical location and seasonal insolation, effects of clouds on the total surface heat budget can be very different. In the Arctic, cloud cover keeps long-wave radiation from being lost to the outer space and consequently raises sea ice surface temperature like the ‘blanket effect’ [Nghiem, 1999]. The amount of short-wave radiation is insignificant while the cloudiness average is 0.65 [Moritz and Perovich, 1996], and the net radiation is larger under overcast skies by $30 \text{ W}\cdot\text{m}^{-2}$ compared to that under a clear sky [Doronin, 1969]. In late spring, the all-wave net flux difference measured over sea ice in the Canadian Arctic Archipelago is in the same order of magnitude [Barber and Thomas, 1998].

At lower latitudes during spring or summer, clouds shield short-wave insolation from the ice surface and thus reduce surface temperature like the ‘umbrella effect’ [Nghiem, 1999]. Starting as early as May in the Arctic, clear sky areas receive a larger net radiation balance [Doronin, 1969]. Furthermore, diurnal warming in ice surface temperature is observable with satellite sensor over sea ice subject to permissible cloud conditions [Ikeda, 1989]. These studies demonstrate the temporal and spatial interdependences of the surface energy balance, albedo, and surface temperature.

The simplified ‘blanket’ and ‘umbrella’ scenarios are further complicated by climatic and dynamic interactions in the total system. With the consideration of albedo-radiation interactions, the shortwave and longwave perturbations may cancel in the surface energy balance for a typical summer albedo [Moritz and Perovich, 1996]. However, the resultant temperature changes should represent the overall effects on sea ice thermal states. Temperature is considered as a leading climatic state variable and temperature changes characterize climatic changes [Antonov and 50 others in Russian Academy of Sciences, 1995]. Monitoring temperature changes and their dynamics in time and in space demands the use of satellite sensors.

3. *A New Approach*

To evaluate the overall effects of clouds in polar regions, it is necessary to observe sea ice surface temperature changes under both cloud-covered and cloud-free conditions. The challenge is that traditional methods for surface temperature measurements, using satellite visible-infrared radiometers, fail under cloudy conditions. In this paper, we present the principle, the mechanism, and the validity conditions of a new approach for microwave radar remote sensing of sea ice surface thermal variations through cloud cover. We show both laboratory and field experiment results. From laboratory experiments at the Cold Regions Research and Engineering Laboratory (CRREL), we investigate the sensitivity of sea ice backscatter to temperature and the dependence of backscatter change on the thermal regimes of sea ice thermodynamic states. Then from the C-ICE field experiment in the Canadian Arctic Archipelago, we demonstrate the use of a C-band radar, which can see through clouds, for remote sensing of sea ice thermal changes using ERS-1 satellite SAR data in conjunction with in-situ measurements together with concurrent AVHRR images for cloud observations.

II. GEOPHYSICAL RELATIONSHIP OF BACKSCATTER AND TEMPERATURE

Spaceborne imaging radars such as the current ERS and RADARSAT SARs or the future ENVISAT and RADARSAT-II SARs, all operating at C band, have the capability to see through clouds and darkness to probe near-surface conditions of sea ice from local to regional scales. The question is whether C-band backscatter from sea ice is related or sensitive to surface thermal states. In this respect, we conducted controlled experiments at CRREL to determine the relationship between C-band radar signatures and sea ice thermal conditions.

The first clear evidence of the relationship between C-band backscatter and sea ice surface temperature for the cold temperature regime below the mirabilite crystallization point has been published [Nghiem *et al.*, 1998]. A crystallization point is defined as the temperature of initial salt formation in sea water brine [Weeks and Ackley, 1982]. Earlier works did not show a conclusive dependence of radar backscatter on ice surface temperature [Swift *et al.*, 1992, Onstott, 1992], furthermore, their results are for X to Ka bands, which are much higher frequencies and are not applicable to the satellite C-band SARs.

Here, we study the dependence of C-band backscatter on sea ice surface thermal states over the temperature regime above the mirabilite crystallization point. We compare the new experimental data with our earlier work [Nghiem *et al.*, 1998] and present the complementary results from the CRREL experiments over both regimes of sea ice surface temperature.

1. *Experimental Setup and Data Collection*

The experiment was conducted at CRREL in February 1995. The ice sheet was grown in the CRREL Geophysical Research Facility (GRF) pond, which is 18.3-m long, 7.62-m wide, and 2.14-m deep as illustrated in Figure 1. The pond was filled with water of 30‰ salinity produced from a mixture of salts composed of sodium chloride (NaCl, 23.98 kg · m⁻³), magnesium chloride (MgCl₂, 3.27 kg · m⁻³), magnesium sulfate (MgSO₄, 1.50 kg · m⁻³), calcium sulfate (CaSO₄, 1.10 kg · m⁻³), potassium sulfate (K₂SO₄, 0.70 kg · m⁻³), and calcium carbonate (CaCO₃, 0.10 kg · m⁻³). These salt fractions are typical of natural sea water [Neumann and Pierson, 1966] but not including traces of potassium bromide (KBr), strontium sulfate (SrSO₄), and boric acid (H₃BO₃), totalling a minute amount of about 0.1‰ by weight.

The Jet Propulsion Laboratory (JPL) C-band polarimetric scatterometer was

mounted about 4 m above the sea ice surface on a gantry that could be moved along the side of the GRF (see Figure 1). The scatterometer is an accurate radar consisting of a diagonal horn antenna, a radio-frequency (RF) subsystem, and a controller subsystem. The antenna mounted on a motorized positioner is shown in Figure 2. The insulated white box above the antenna contained the temperature-controlled RF subsystem. Wrapped in a heating pad located below the antenna is a video camera pointed in the same direction as the antenna. The controller subsystem, including a computer for radar control and data acquisition, was housed in a heated tent at a corner of the GRF. During data acquisitions, the scatterometer operator could view the target area on a TV monitor connected to the video camera as the antenna scanned across and along the sea ice sheet. A calibration site was setup on the walkway next to the GRF for calibration measurements with a metallic sphere and a trihedral corner reflector. Detailed descriptions of the polarimetric scatterometer, system calibration, data acquisition, and data processing have been presented elsewhere [Nghiem *et al.*, 1997a, 1997b, 1998].

In conjunction with radar measurements, physical property measurements were made to characterize the sea ice, including its thickness, crystallographic structure, salinity profile, and temperature profile. Air, ice, and water temperatures were measured with a thermistor string located at the far end of the GRF and were recorded with a computer in the pump house (see Figure 1). At the other end of the GRF, a hand-held digital thermometer was used before and after each set of radar measurements to take air temperatures at a height of approximately 1.3 m and temperature near (within 1 cm above) the ice surface. Moreover, a CRREL meteorological station, located about 250 m northeast of the GRF and elevated 15 m above the GRF, was operated to monitor environmental conditions. The station sensors and data collection have been described by the CRREL Meteorological Team [U. S. Army TECOM Hanover Meteorological Team, 1994]. The me-

eteorological data set includes air temperature, short-wave and long-wave radiation, wind speed, and wind direction.

2. Environmental Conditions

Figure 3 presents meteorological conditions during the scatterometer measurement period over a full day cycle from 6 am local time on the 19th to the same time on the 20th of February 1995. Short-wave insolation began a little before 7 am and peaked up sharply before 10 am on 19 February when a period of significant cloud overcast started. The partly overcast sky condition is also seen in the photograph in Figure 2. The cloudy sky period during the daytime resulted in a significant loss of short-wave radiation represented by the daytime dip plotted in the top left panel of Figure 3. The incident short-wave radiation diminished during the afternoon and died out a little before 6 pm in the evening. The incident long-wave radiation in the top right panel of Figure 3 shows similar trend during the day time without the daytime dip due to long-wave energy emitted from the cloud cover. The long-wave plot reveals an interesting peak before midnight by the end of 19 February as seen in Figure 3. This could be caused by clouds with a warmer air mass passing through the local area, corresponding to the increase in wind speed recorded at the same time as shown in the wind-speed plot in the lower left panel of Figure 3. Then, the long-wave radiation decreased during the early hours of 20 February.

Air temperature at the meteorological station is plotted in the lower right panel of Figure 3. The temperature closely indicates the above thermal environments. First, the temperature started to rise at the beginning of the insolation and increased sharply along with the short-wave radiation. The slope of the temperature curve breaks at about 10 am corresponding to the onset of overcast cloud conditions. The temperature continued to increase at a slower rate during the late morning and early afternoon hours when the

insolation loss was compensated by the gain in long-wave radiation. The short period of local warming before midnight is also observed in the temperature curve. During the early hours of 20 February, the temperature steadily decreased in concert with decreasing long-wave radiation.

The thermal response over the sea ice sheet is described by temperature measurements plotted in Figure 4. At the far end of the GRF, temperatures measured by thermistors at 8 cm ($T_{8\text{ cm}}$) and 3 cm ($T_{3\text{ cm}}$) above the sea ice surface shows a similar trend as shown in the left panel of Figure 4. Note the cloud overcast effects and the midnight warming in the thermistor temperature curves. Temperatures measured with the digital thermometer near the radar measurement site also revealed a similar thermal response as presented in the right hand panel of Figure 4. Temperatures T_{air} at about 1.3-m height and T_{ice} within 1 cm above the ice surface show more small variabilities due to measurements uncertainties with the hand-held thermometer. The thermometer and thermistor data were not cross calibrated; however, the two sets of temperature data exhibit the same thermal response to the fast initial heating, the slow-down due to cloudy sky, the midnight warming, and the cool-down in the early morning.

3. Sea Ice Characteristics

The sea ice sheet was 34-cm thick when scatterometer measurements began. Ice cores through the entire thickness were retrieved for salinity profile measurement and ice crystal structure studies. The salinity profile shown in Figure 5 is typical of sea ice salinity distribution, characterized by a high salinity (14⁰/∞) just beneath the upper surface of the ice sheet followed by much reduced salinity (3-5⁰/∞) in the interior of the ice sheet and a higher salinity (7⁰/∞) at the interface with the sea water.

The thermal response within the ice sheet is shown in Figure 6 for 12 different thermal

states for every two hours throughout a full day period. Temperature profiles (continuous curves in Figure 6) measured with the thermistor string show a strong response to the thermal forcing in the upper 10 cm of the ice sheet. As observed in Figure 6, the upper ice temperature followed the warming and cooling cycles corresponding to the variations in radiation fluxes (see Figure 3) throughout the day. Note that temperatures near the air interface were above the mirabilite crystallization point in all cases. The temperature changed little in the middle layer and practically remained constant near the interface of the sea ice with the sea water.

From the salinity and temperature profiles, brine volume distributions in the sea ice sheet are determined [Cox and Weeks, 1983] for different thermal states. The results plotted in Figure 6 show that the brine volume changed significantly in the upper few centimeters of the ice sheet due to the high salinity and large thermal variations in the surface layer of the ice sheet. These large changes in the upper ice layer driven by the thermal forcing are important to the scattering mechanism responsible for the sea ice backscatter signature at C-band as discussed in a later section of the paper.

As brine volume increases with increasing temperatures in the ice, the volume of an individual brine pocket increases by pocket wall melting in order to account for the eutectic phase change [Weeks and Ackley, 1982]. Effects of temperature on brine pocket size have been studied by Perovich and Gow [1991]. Thus, part of the radiation energy is absorbed at the surface to enlarge brine pockets [Moritz and Perovich, 1996]. During the process of brine pocket enlargement, brine interconnections begin to appear, leading ultimately to the formation of brine channels. Brine channel formation, occurring as a result of thermal effects, was observed during the experiment.

Photographs of brine channels in Figure 7 were taken by a hand-held camera looking perpendicularly down to the surface of the ice sheet. The top photograph shows a few

groups of brine channels and the bottom photograph is a closeup shot of the brine channels located in the middle section of the upper part of the top photograph. Characteristics of the crystallographic structures in the sea ice sheet are shown in Figure 8. The vertical thin sections (corresponding to the 34-cm thickness of the ice sheet) on the left of Figure 8 show the columnar structure underlying a frazil ice layer formed during the initial stages of the ice growth. Vertical brine channels are also seen in these thin sections. Horizontal thin sections (1.6 cm from left to right side of the photographs) on the right of Figure 8 show: the granular nature of the frazil structure at the top of the ice sheet, rounded texture at 10 cm and 20 cm indicative of thermal modifications, and typical platelet structure at 32 cm. A few brine inclusions can be observed in these horizontal thin sections. Changes in the physical characteristics of sea ice under thermal response presented in this section will be used to explain the observed backscatter signature.

4. Relationship of Sea Ice Backscatter and Temperature

Throughout the warming and cooling cycles, sea ice backscatter was monitored with the Jet Propulsion Laboratory C-band polarimetric scatterometer at incident angles from 20° to 35° for all horizontal (h) and vertical (v) polarization combinations. To investigate the response of C-band backscatter signature to the thermal states of sea ice, we compare the backscatter change in the time-series radar measurements with the evolution of the temperature over the sea ice surface.

4.1. Copolarized Backscatter versus Temperature

For copolarized backscattering coefficients σ_{hh} and σ_{vv} versus temperature T_{sur} near the ice surface, the results are shown in Figure 9 where backscatter data are represented by symbols (square for σ_{hh} and triangle for σ_{vv}) connected with continuous lines and the

measurement uncertainties are denoted with the vertical bars. The background colors in each plot correspond to surface temperature T_{sur} at the local time shown in the horizontal axis. The initial low backscatter in the early morning of February 19 sharply increased in response to the strong increase in temperature (deep blue to orange). At about 10 am, the backscatter tapered off as a result of the weak change in temperature (different shades of orange color) due to the cloud overcast. Backscatter peaked shortly after the noon time with the warm temperature, and then decreased during the afternoon and evening along with the decreasing temperature.

Note the small peak in the backscatter curves shown in Figure 9 at the time corresponding to the short midnight warming period. The midnight backscatter peak is higher at 20° incident angle, smaller at 25° , and not seen at 30° and 35° . A possible explanation is that the target area at 20° was on the ice at the near side of the scatterometer where T_{sur} shown a clear midnight warming effect (curve with close black circle in the right panel of Figure 4). For the larger incident angles, the target areas are closer to the far side of the sea ice sheet where the midnight warming effect is hardly seen in the temperature measured near the ice surface (dotted curve for T_{3cm} in the left panel of Figure 4). After the midnight peak, backscatter became low during the cold early hours of the next day (20 February).

As observed in Figure 9, both σ_{hh} and σ_{vv} are well correlated to and follow exactly the same trend of the diurnal thermal response over the sea ice sheet. The backscatter is positively correlated to temperature and the process is reversible with short-term thermodynamic variations such as the daytime warming and the nighttime cooling of sea ice. These results are consistent with our previous study of diurnal effects [Nghiem *et al.*, 1998]. Furthermore, the backscatter change is very sensitive to the thermal change in this experiment. The change in the backscatter varies as much as 10 dB, that is one order

of magnitude, from the warm case about noon on 19 February to the cold case in early morning of 20 February. Over this time period, we carry out an analysis of the backscatter and temperature data with the linear regression.

Table 1 shows the results for backscatter and temperature T_{sur} for all of the polarizations and incident angles. In the table, α is the slope for the linear relationship between backscatter and temperature, β is the bias between the two quantities, δ is the variance, and ρ_c is the correlation coefficient. For horizontal backscatter σ_{hh} in Table 1a, the backscatter change is about 1.1 dB per 1°C variation in temperature for all of the incident angles while β is a decreasing function of incident angle with a variance of 1.5 dB for most cases. Except at $\theta = 35^\circ$ where $\rho_c = 0.76$, the correlation coefficient ρ_c is as high as 0.84 or better, indicating a good correlation between backscatter and surface temperature over the ice. Similar results hold for the relationship between σ_{vv} and T_{sur} with ρ_c equal or better than 0.8 as shown in Table 1b.

Table 2 lists the results for the relationship between backscatter and air temperature T_{air} at the height of approximately 1.3 m average above the sea ice surface. Estimated from Table 2a, the average sensitivity between σ_{hh} and T_{air} is 0.48 dB per degree C with an average variance of about 1 dB and a decreasing trend in β for larger incidence angles. For σ_{vv} and T_{air} (Table 2b), the average sensitivity is 0.52 dB per degree C. For both polarizations, the backscatter is very well correlated with the temperature with high values of correlation coefficient ρ_c ranging from 0.88 to 0.96 for all of the incident angles.

4.2. Polarimetric Backscatter versus Temperature

Polarimetric backscatter signatures are plotted in Figure 10 over the color background representing the diurnal cycle of surface temperature T_{sur} . The polarimetric parameters, denoted by symbols connected with continuous curves in Figure 10, include copolarized

ratio $\gamma = \sigma_{vv}/\sigma_{hh}$, crosspolarized ratio $e = \sigma_{hv}/\sigma_{hh}$, magnitude and phase of complex correlation coefficient $\rho = \sigma_{hhvv}/\sqrt{\sigma_{vv}\sigma_{hh}}$. There are 16 panels for the four polarimetric parameters at four different incident angles.

The four panels in the top row of Figure 10 show the results for copolarized ratio γ . The ratio varies within ± 2 dB, and there is no obvious signature response to the diurnal warming and cooling cycles. However, the curves indicate a weak dip corresponds to the midnight warming period at incident angles 20° , 25° , and 30° . These results suggest that the horizontal backscatter has a larger increase during the midnight warming period compared to a weaker increase in the vertical backscatter.

Crosspolarized ratios are plotted in the second row of Figure 10. The experimental curves exhibit a clear depression during the daytime warm insolation period. This is because copolarized backscatter σ_{vv} has a strong increase while crosspolarized backscatter σ_{hv} is insensitive to the thermal change. To the first order, crosspolarized backscatter is more affected by the scatterer shape [Nghiem *et al.*, 1995a, 1995b]. This result suggests that the thermal cycles have a weak effect on the scatterer shape distribution.

Polarimetric correlation coefficient ρ is presented in the third row of Figure 10 for the magnitude and in the last row for the phase. There is no conclusive signature in both magnitude and phase of ρ at 20° - 30° incident angles over different phases of the diurnal cycle. This result is not surprising because the incidence angles are not large and the decorrelation effect between horizontal and vertical polarizations is weak [Nghiem *et al.*, 1995a, 1995b]. For small incident angle near nadir looking, there is not much distinction between horizontal and vertical polarizations and the returns are expected to be well correlated. At the larger incident angle at 35° , magnitude of ρ , however, has lower values during the daytime warming, and also show a weak dip corresponding to the midnight warm period as seen the rightmost panel in third row of Figure 10.

In general, the diurnal thermal effects are observed strongly in copolarized backscatter σ_{hh} and σ_{hh} with a good sensitivity and correlation with temperature over sea ice. Polarimetric signatures including the above parameters at small incident angles do not show a clear relationship with different sea-ice surface thermal conditions.

4.3. Backscatter Response in Different Thermal Regimes

The above results show a very sensitive backscatter signature to temperature. In this experiment, sea ice temperature was above the mirabilite ($\text{Na}_2\text{SO}_4 \cdot 10\text{H}_2\text{O}$) crystallization point (-8.2°C). Another experiment was carried out at CRREL in the winter of 1994 to study diurnal thermal cycling effects on sea ice polarimetric backscatter [Nghiem *et al.*, 1998]. The same JPL C-band polarimetric scatterometer was used to measure backscatter from a sea ice sheet grown from saline water with the same salt mixture. In the 1994 experiment, sea ice temperatures were at or below the mirabilite crystallization temperature but above the the crystallization point of $\text{MgCl}_2 \cdot 8\text{H}_2\text{O}$ (-18.0°C). Over these two distinctive thermal regimes of sea ice, we compare the backscatter changes at both horizontal and vertical polarizations over the range of incident angle from 20° to 35° as shown in Figure 11.

The comparison in Figure 11 shows strong backscatter changes by 8 to 10 dB, represented by the left vertical bar (light grey) at each incident angle, for the sea ice thermal regime above the mirabilite crystallization point. For the lower thermal regime, the backscatter also shows significant changes (dark grey vertical bars in Figure 11) with temperature; however, the backscatter changes are smaller and ranges from 4 to 6 dB. In both experiments, the change in sea ice temperature is approximately 8°C . These results clearly show distinctive slopes of backscatter as a function of temperature over the two different thermal regimes of sea ice thermal states. The same conclusion holds for both horizontal

backscatter σ_{hh} and vertical backscatter σ_{vv} as seen in Figure 11.

The observations from the two experiments suggest that the backscattering of electromagnetic waves at C band is related to the temperature which determines the thermodynamic distribution of brine volume in the sea ice surface layer. We plot the brine volume in sea ice as a function of ice temperature [Cox and Weeks, 1983] in Figure 12. The curves from the lowest to the highest are for every 2 ‰ increment in salinity ranging from 4 ‰ to 16 ‰. On the brine volume curves, we denote the crystallization points of $\text{CaCO}_3 \cdot 6\text{H}_2\text{O}$ with triangles, $\text{Na}_2\text{SO}_4 \cdot 10\text{H}_2\text{O}$ (mirabilite) with squares, and $\text{MgCl}_2 \cdot 8\text{H}_2\text{O}$ with circles. The curves show changes in brine volume as determined by the thermodynamic eutectic phase distribution in sea ice over the two thermal regimes. Above the mirabilite point, the brine volume curves have slopes that are distinctively larger than those in the lower thermal regimes. These trends correspond well with the observations of the backscatter changes above. These results further verify the relation of sea ice backscatter with brine volume as observed earlier by Nghiem et al. [1998].

III. ARCTIC FIELD EXPERIMENT RESULTS

1. *Utility of Concurrent C-band SAR and Optical-Infrared Sensors*

The vast areal extent of sea ice necessitates the use of satellite sensors. Current active C-band SAR in low earth orbits such as ERS or RADARSAT has a high resolution (30-100 m) applicable to the local scale (hundreds of meters). The passive optical sensor AVHRR has a resolution of 1.1 km at nadir (Local Area Coverage data), which is comparable to the local scale and is one order of magnitude finer than the aggregate scale of tens of kilometers [Moritz and Perovich, 1996].

Furthermore, the coverages of the satellite sensors are large because of wide swath

widths (100 km for ERS, \sim 500 km for RADARSAT, and 2900 km for AVHRR) covering the regional scale (100's of km). Since C-band SAR sees through clouds, backscatter data can be used to observe sea ice surface temperature changes under both cloud covered and cloud free conditions. On the other hand, optical and infrared AVHRR sees clouds. This approach effectively utilizes the sensitivity of C-band backscatter to the temperature and the ability of C-band radar to see through clouds while concurrent AVHRR data are used for cloud detection and identification. In the following sections, we present an example from the Canadian C-ICE (Collaborative-Interdisciplinary Cryosphere Experiment) field experiment together with ERS SAR and AVHRR data to determine changes in Arctic sea ice surface thermal states and effects of cloud cover on the surface energy balance.

2. *The C-ICE Field Experiment*

Long-term field experiments have been carried out in the past decade (1990-1999) for in-situ process studies near Resolute Bay, Nunavut Canada. Detailed surface data were used to investigate the relationship between geophysical parameters and radar backscatter [Barber *et al.*, 1994, 1996, 1998]. These studies indicated there exists a relationship between time-series backscatter and physical aspects that control the temperature regime. In this paper, we use in-situ data obtained during the 1993 experiment. C-ICE is a multidisciplinary research program conducted annually from Resolute Bay in the central region of the Canadian Arctic Archipelago. The 1993 site was located between Griffith and Cornwallis Islands, over which concurrent satellite SAR and visible-infrared data were acquired.

Over the period from 22 April to 20 June 1993, physical, electrical, and energy balance variables were measured at a first-year sea ice site. Towers for energy balance measurements were stationed over both first-year and multi-year sea ice sites. Energy balance components were recorded as 15-minute averages by Campbell Scientific Instruments

data loggers. The two sites were instrumented for temperature profile measurements with thermocouple sensors embedded in snow and sea ice. Physical properties of sea ice were acquired from ice cores. Salinity, density, and temperature were measured in situ from the extracted cores. Vertical and horizontal thin sections similar to those in Figure 8 were used to examine details of ice microstructure. Digital analyses of the thin sections provide fractional volumes, size, and shape of the inhomogeneities over the vertical dimension of the ice core. In early May, snow depths at the temperature profiling sites were 12 cm for the first-year ice site and 24 cm for the multi-year ice site. Physical properties of snow including grain size distribution, density, and salinity were obtained from snow pits located within an area immediately adjacent to a thermocouple array associated with the two microclimate stations.

3. AVHRR Observations of Cloudy and Clear Conditions

The Advanced Very High Resolution Radiometer (AVHRR) aboard NOAA satellites is a cross-track scanner that measures electromagnetic radiation from the visible to infrared regions at five channels, namely: 0.55-0.68 μm (channel 1), 0.725-1.10 μm (channel 2), 3.55-3.93 μm (channel 3), 10.3-11.3 μm (channel 4), and 11.5-12.5 μm (channel 5). Channels 1 and 2 are in the visible wavelengths and used for albedo estimates and cloud masking, channels 4 and 5 are thermal infrared channels used for surface temperature estimates and cloud masking, while channel 3 is an intermediate channel used mainly for cloud masking. The resolution of the basic data, which is sometimes referred to as Local Area Coverage (LAC) or High Resolution Picture Transmission (HRPT), is about 1 km^2 at nadir, while at other scan angles, the resolution degrades. There are 2048-pixels in each scan, covering a swath width of 2700 km.

Over open ocean, the discrimination between cloud-free and cloud-covered areas is

facilitated by the large contrast in the albedo and emissivity of clouds and those of water. However, over sea ice, the discrimination is more difficult because of the presence of cold snow cover that substantially reduces the contrast in the albedo and emissivity of clouds and the surface [Yamanouchi *et al.*, 1987, Allison *et al.*, 1993]. AVHRR images during cloud free (6 May 1993) and cloudy (9 May 1993) conditions in the study area, are shown in Figure 13 and 14 for infrared and visible data, respectively. The arc line across the AVHRR images passing through Cornwallis Island corresponds to 75°N latitude.

In these images, cloud covered areas are recognized by a largely variable spatial pattern and relatively low temperatures. The radiances, converted into brightness temperatures, are usually higher over sea ice surfaces compared to cloud tops (except when there is inversion). For example, the cloud tops in Figure 13b, are shown to have temperatures that are about 10K lower than corresponding cloud free regions in Figures 13a. In the cloud free portion of the sea ice cover, the temperatures are also shown to be below but close to melting temperatures as expected during early spring in the Arctic. In the visible channel (Figures 14a and 14b), the corresponding images show the cloud patterns more distinctly. In this channel, it is also possible to identify different types of clouds since the albedo of clouds changes from 0.2 to 0.7 depending on cloud types.

Some techniques for retrieving surface temperatures over snow and ice from AVHRR and Temperature Humidity Infrared Radiometer (THIR) have been reported [Comiso, 1983, Key and Haeffliger, 1992, Comiso, 1994, Massom and Comiso, 1994, Key *et al.*, 1997]. The accuracy in the retrieval of surface skin temperatures from satellite infrared data depends strongly on the success in cloud masking. With AVHRR data, cloud masking is usually done by a thresholding technique that utilizes one of the visible channels or the difference between channels 3 and 4 and/or between channels 4 and 5. When channel 3 data are utilized, a noise reduction procedure [Simpson and Yhann, 1994] is applied to the

data because of substantial instrumental noise at low temperatures. Another technique, which we call daily differencing method takes the difference of daily orbital data and uses a threshold, based on the change in observed radiances due to the movement of clouds.

The method we found to be most effective in the polar environment is a combination of all these techniques with emphasis on the use of the daily differencing method using channel 4 data and the difference of channels 3 and 4 data. The surface temperature is then inferred using regression techniques that makes use of surface data and the difference of channels 4 and 5 that corrects for spatial variations in water vapor effects. Since sea ice is usually covered by snow the emissivity of which is close to unity, errors associated with spatial variations of emissivity is small. Both infrared and visible results from AVHRR show that the experimental area was clear (zero cloud mask) on 6 May 1993 and completely cloudy (100% cloud mask) on 9 May 1993 in agreement with direct field observations.

4. ERS-1 SAR Observations of Temperature Change

ERS 1 carried a C-band SAR (5.3 GHz) which measured backscatter from geophysical media of the earth. ERS-1 satellite was in a sun-synchronous and near-polar orbit with a mean altitude of 785 km. ERS-1 SAR transmitted and received vertically polarized waves and σ_{vv} data were collected. The SAR looked to the right of the spacecraft at an average incidence angle of 23° , which is within the range of incident angles of the results presented in section II. The swath of ERS-1 SAR images was 100 km with a pixel spacing of 100 m. ERS-1 SAR data were processed at the Alaska SAR Facility in Fairbanks, Alaska. The data were calibrated to backscattering coefficient σ_{vv} according to Olmsted [1993].

Figure 15 presents the results observed with ERS-1 SAR data. The Griffith and Cornwallis Islands are seen in the image. Figure 15a shows the original ERS-1 image of sea ice at C-ICE site together with field experiment data for ice and snow thicknesses at

different area corresponding to different consolidation periods from September to March during the sea ice season. The study area was segmented into the four periods with archived ERS-1 SAR data from the accretion period, ice charts from the Canadian Ice Services, and in-situ observations from a reconnaissance field sampling program between April and June 1993.

Figure 15b is the image of the backscatter difference between two repeat passes of ERS-1 SAR. The islands have been excluded by the image processing algorithm and replotted with the original data in the processed image for a clear presentation of the island appearances. The resulting image is derived from two colocated ERS-1 images acquired at nighttime on 6 May and 9 May. To observe the spatial distribution of backscatter change (0.5-2.5 dB) over the experimental area, the Gaussian filtering and image contouring have been applied. The resultant image shows backscatter increases under cloud cover compared to the clear-sky case. Further details of these results are presented elsewhere [*Barber and Nghiem, 1999*].

The results in Figure 15b lead to several conclusions on the sea ice surface thermal states under cloud effects over this area. First, the cloud cover at nighttime has a 'blanket effect' that increases sea ice surface temperature corresponding to the backscatter increase. Similar 'blanket effect' has been observed directly with in-situ measured results of temperature, cloud cover, and energy balance from the Surface Heat Budget of the Arctic Ocean (SHEBA) [*Perovich et al., 1999a*], a year-long intensive field experiment carried out in 1997-1998. Thus, C-ICE and SHEBA indicate that the 'blanket effect' can consistently occur on both stationary landfast sea ice (C-ICE) and drifting pack ice (SHEBA). Field measurements show an increase of more than $30 \text{ W} \cdot \text{m}^{-2}$ in the all-wave net radiation over first-year sea ice, which confirms the 'blanket effect' of cloud cover on the surface energy balance which increases the surface temperature and backscatter as observed with SAR

data [*Barber and Thomas, 1998, Barber and Nghiem, 1999*].

Second, larger surface temperature change observed with larger backscatter change over sea ice area corresponding to later consolidation periods (compare the September, November, and January consolidation areas in Figure 15). Such results map out areas of more importance to thermal energy transfer and thus more influence on the surface heat budget balance. Third, within a given area of consolidation, the contoured map represents the statistics of sea ice surface temperature response to the cloud cover. This occurs because of the role which snow thermal diffusivity plays in controlling the snow and ice interface temperature between a cloudy and clear atmosphere [*Barber and Thomas, 1998, Barber and Nghiem, 1999*]. Different temperature responses may be caused by different snow thickness which affects the temperature at the surface between snow and sea ice. Nevertheless, it is the resulting ice surface temperature that determines brine volume distribution in both sea ice and snow near the boundary interface, causing changes in the observed backscatter. The change in snow-ice interface temperature is a direct consequence of the surface energy balance. Since backscatter is closely related to this temperature, backscatter measurements can be used to determine the energy balance.

Furthermore, note a multi-year ice floe in the January consolidation area. This floe is located above characters 'ol' in the string 'Jan. Consolidation' in Figure 15a. The backscatter difference image in Figure 15b shows no change exactly at this location; this is because multi-year sea ice does not contain enough salinity for the effect to be observable as required by the scattering mechanism related to brine volume presented in section II. Another observation is the lack of backscatter change in the March consolidation area (area 5). However, there was no detailed field data to determine the scattering mechanism nor the thermal environment in this area [*Barber and Nghiem, 1999*]. During summer, the ice surface is wet due to pervasive melt on sea ice, C-band attenuation becomes large,

and C-band backscatter is more sensitive to the surface roughness. In this case, surface temperature should stay relatively constant at the melting point under the isothermal condition, and it is not critical nor practical to observe sea-ice surface temperature during the summer melt process.

The method to observe sea ice thermal states presented in this paper is applicable to first-year ice but not for multi-year ice. Nevertheless, the approach is valid in two aspects. First, the heat transport through first-year and young sea ice ranges one to two orders of magnitude larger than that through perennial ice, the energy exchange rate is very sensitive to boundary layer thermal conditions, and the contribution to the total thermal energy input into the atmospheric boundary layer through young ice is significant compared to that from regions of thick multi-year ice [*Maykut, 1978*]. Second, Arctic sea ice is very dynamic and ice motion creates ice divergence areas in the ice pack where first-year and young ice forms. First-year sea ice in divergence areas, distributed over the ice pack and not just near the ice edge, serves as a distributed network of ‘natural stations’ to observe the surface energy balance under cloudy and clear conditions. SAR and optical-infrared sensors have the necessary resolutions for such application.

V. SUMMARY AND DISCUSSION

This paper presents a study of surface thermal states over first-year sea ice under cloud cover with satellite C-band SAR and visible-infrared sensors. From controlled laboratory experiments, we show that C-band copolarized backscatter is very well correlated and sensitive to surface temperature of first year sea ice. Experimental results reveal that the backscatter change for a given surface temperature change depends on the thermal regime of sea ice. For the regime above the mirabilite crystallization point, the backscat-

ter change can be as much as 10 dB (one order of magnitude) for an approximately 8°C change in temperature. Over the thermal regime between mirabilite and $\text{MgCl}_2 \cdot 8\text{H}_2\text{O}$ crystallization points, the backscatter change is between 4-6 dB for about the same change in temperature. These results indicate that the backscattering of electromagnetic waves at C band is related to the temperature which determines the thermodynamic distribution of brine volume in the sea ice surface layer.

Based on the relationship of C-band backscatter to sea ice surface thermal conditions, we use satellite SAR for the observation of sea ice surface temperature change and energy balance under cloud cover together with concurrent visible-infrared data for cloud detection and identification. Furthermore, measurements at the C-ICE site provide in-situ geophysical data for sea ice, snow, energy balance, and other environmental parameters. ERS-1 SAR backscatter differences between cloudy and clear sky (determined by AVHRR) dates show an increase in backscatter with a distribution consistent with different consolidation periods of sea ice. The results show that cloud cover results in a net positive surface energy balance, as verified with C-ICE in-situ measurements, causing an increase in ice temperature by the 'blanket effect'. The method is applicable to first-year ice areas, where the heat flux is strong and the contribution to the total energy balance is significant. In this respect, the distribution of first-year sea ice over different regions serves as a network of natural observation stations.

An advantage of the C-ICE field experiment is that the experiment was located in a region of stationary landfast ice. In general, sea ice is dynamic with complicated motions and deformations causing ice drifting, convergence, and divergence. The National Aeronautics and Space Administration (NASA) has invested in the development of a complex system to track ice motion, deformation, thickness, and ice age together with time-series C-band backscatter and other physical parameters. The system, known as the RADARSAT

Geophysical Processing System (RGPS) [*Kwok et al.*, 1995, 1999], has been implemented by the Jet Propulsion Laboratory and is currently operational at the Alaska SAR Facility. RGPS is particularly designed for use with the Canadian RADARSAT-1 SAR data. This SAR is also operated at C band but with a larger swath and coverage compared to ERS SAR. Furthermore, RADARSAT data have been collected over the SHEBA site, providing both satellite and in-situ data [*Perovich et al.*, 1999b] colocated in time and in space for further study, validation, and application to the observation of sea-ice thermodynamics and energy balance under cloud effects. ENVISAT C-band SAR (planned by the European Space Agency for a near-future launch for a five-year mission) data are also appropriate for the monitoring of Arctic sea ice surface thermal states under various cloud conditions.

ACKNOWLEDGMENTS

The research described in this paper was performed by the Jet Propulsion Laboratory, California Institute of Technology, and was sponsored by the Office of Naval Research (ONR) and the National Aeronautics and Space Administration. The research by the U. S. Army CRREL was funded under ONR contracts N00014-95-MP-3002 and N00014-95-MP-3019. The research by the University of Manitoba was supported by the Canadian Ice Service, the Natural Sciences and Engineering Research Council of Canada, and grant N00014-94-1-03-86 from the Office of Naval Research. The assistance of Bruce Elder and John Govoni in the CRREL experiments is gratefully acknowledged.

REFERENCES

- Allison, I., R. E. Brandt, and S. G. Warren, East Antarctic sea ice: Albedo, thickness distribution, and snow cover, *J. Geophys. Res.*, **98**(C7), 12,417-12,429, 1993.
- Ambach, W., The influence of cloudiness on the net radiation balance of a snow surface with a high albedo, *J. Glaciol.*, **13**, 73-84, 1974.
- Antonov, V. V., N. A. Armand, L. P. Bobylev, F. V. Bunkin, V. V. Viter, A. M. Volkov, K. I. Volyak, P. M. Vorobyev, S. N. Voyakin, A. A. Galeev, A. P. Galtsev, N. F. Glazovskii, G. G. Golitsyn, I. S. Gorelik, G. M. Grechko, A. S. Gurvich, Yu. S. Degterev, Yu. S. Denisov, E. S. Dmitriev, V. M. Egorov, N. F. Elanskii, G. A. Efremov, V. B. Zalesnyi, Ya. L. Ziman, V. V. Zuev, V. E. Zuev, A. L. Knipper, O. I. Kozlov, K. Ya Kondrat'ev, V. M. Kotlyakov, Yu. A. Kravtsov, B. G. Kutuza, O. N. Lebedev, G. G. Matvienko, S. S. Moiseev, M. A. Naumenko, L. B. Neronskii, V. P. Nefediev, I. G. Osipov, L. A. Pakhomov, V. N. Pelevin, V. A. Rumyanzev, L. A. Savostin, A. S. Sarkisian, Yu. P. Semenov, I. A. Strukov, V. G. Trifonov, Yu. V. Trifonov, A. I Chavro, P. A. Shirokov,

- and V. S. Etkin, *Space Studies of the Earth as an Ecological System and the Human Impact on this System*, Russian Academy of Sci., Space Res. Inst., "ECOS" Prog.: Ver. 2, Pr-1907, 71 pp., 1995.
- Barber, D. G., T. N. Papakyriakou, and E. F. LeDrew, On the relationship between energy fluxes, dielectric properties, and microwave scattering over snow covered first-year sea ice during the spring transition period, *J. Geophys. Res.*, **99**(C11), 22401-22411, 1994.
- Barber, D. G., T. N. Papakyriakou, E. F., LeDrew. and S. Shokr, An examination of the relationship between the spring period evolution of the scattering coefficient (σ_0) and energy fluxes over landfast sea ice, *Int. J. Remote Sens.*, **16**(17), 3343-3363, 1996.
- Barber, D. G., and A. Thomas, The influence of cloud cover on the radiation budget, physical properties and microwave scattering coefficient (σ^0) of first-year and multi-year sea ice, *IEEE Trans. Geosci. Remote Sens.*, **36**(1), 38-50, 1998.
- Barber, D. G., A. Thomas, and T. Papakyriakou, Role of SAR in surface energy flux measurements over sea ice, in *Analysis of Data of the Polar Oceans*, edited by C. Tsatsoulis and R. Kwok, chap. 3, pp. 35-67, Springer-Verlag, Berlin, 1998.
- Barber, D. G., and S. V. Nghiem, The role of snow on the thermal dependence of microwave backscatter over sea ice, *J. Geophys. Res.*, **104**(C11), 25789-25803, 1999.
- Cess, R. D., G. L. Potter, J. P. Blanchet, G. J. Boer, S. J. Ghan, J. T. Kiehl, H. LeTreut, X. Z. Li, X. Z. Liang, J. F. B. Mitchell, J. J. Morcrette, D. A. Randall, M. R. Riches, E. Roeckner, U. Schlese, A. Slingo, K. E. Taylor, W. M. Washington, R. T. Weatherald, and I. Yagai, Interpretation of cloud-climate feedback as produced by 14 atmospheric general circulation models, *Science*, **245**, 513-516, 1989.
- Comiso, J. C., Sea ice effective microwave emissivity from satellite passive microwave and infrared observations, *J. Geophys. Res.*, **88**(C12), 7686-7704, 1983.
- Comiso, J. C., Surface temperatures in the polar regions from Nimbus-7 temperature

- humidity infrared radiometer, *J. Geophys. Res.*, 99(C3), 5181-5200, 1994.
- Cox, G. F. N., and W. F. Weeks, Equations for determining the gas and brine volumes in sea-ice samples, *J. Glaciol.*, 29(12), 306-316, 1983.
- Croll, J., *Climate and Time in Geologic Relations, A Theory of Secular Change of the Earth's Climate*, Isbister and Co., London, 1875.
- Curry, J. A., and E. E. Ebert, Annual cycle of radiation fluxes over the Arctic ocean: Sensitivity to cloud optical properties, *J. Climate*, 5, 1267-1279, 1992.
- Curry, J. A., W. B. Rossow, D. Randall, and J. L. Schramm, Overview of Arctic cloud and radiation characteristics, *J. Climate*, 9(8), 1731-1764, 1996.
- Doronin, Y. P., *Thermal Interaction of the Atmosphere and the Hydrosphere in the Arctic*, Hydrometeorological Institute, Leningrad, 244 pp., 1969. (Trans. by the Israel Prog. for Sci. Pub., Jerusalem, 1970).
- Ikeda, M., Snow cover detected by diurnal warming of sea ice/snow surface off Labrador in NOAA imagery," *IEEE Trans. Geosci. Remote Sens.*, 27(5), 552-560, 1989.
- Ingram, W. J., C. A. Wilson, and J. F. B. Mitchell, Modelling climate change: An assessment of sea ice and surface albedo feedbacks, *J. Geophys. Res.*, 94, 8609-8622, 1989.
- Kellogg, W. W., Climatic feedback mechanisms involving the polar regions, *Proc. Clim. of the Arctic: Twenty-fourth Alaska Sci. Conf.*, 111-116, Geophysical Institute, University of Alaska, 1973.
- Key, J. R., and M. Haeffliger, Arctic ice surface temperature retrieval from AVHRR thermal channels, *J. Geophys. Res.*, 97(D5), 5885-5893, 1992.
- Key, J. R., A. J. Schweiger, and R. S. Stone, Expected uncertainty in satellite-derived estimates of the surface radiation budget at high latitudes, *J. Geophys. Res.*, 102(C7), 15,837-15,847, 1997.

- Kwok, R., D. A. Rothrock, H. L. Stern, and G. F. Cunningham, Determination of ice age using Lagrangian observations of ice motion, *IEEE Trans. Geosci. Remote Sens.*, *33*(2), 392-400, 1995.
- Kwok, R., G. F. Cunningham, N. LaBelle-Hamer, B. Holt, and D. Rothrock, Ice thickness derived from high-resolution radar imagery, *EOS Trans.*, Amer. Geophys. Union, *80*(42), 495-497, 1999.
- Manabe, S., R. J. Stouffer, M. J. Spelman, and K. Bryan, Transient response of a coupled ocean-atmosphere model to gradual changes of atmospheric CO₂, I: Annual mean response, *J. Climate*, *4*, 785-818, 1991.
- Massom, R. and J. C. Comiso, The classification of Arctic sea ice types and the determination of surface temperature using advanced very high resolution radiometer data, *J. Geophys. Res.*, *99*(C3), 5201-5218, 1994.
- Maykut, G. A., Energy exchange over young sea ice in the central Arctic, *J. Geophys. Res.*, *83*(C7), 3646-3658, 1978.
- Moritz, R. E., J. A. Curry, A. S. Thorndike, and N. Untersteiner, Eds., *SHEBA, A Research Program on the Surface Heat Budget of the Arctic Ocean*, Rep. No. 3, U. of Washington, 36 pp., 1993.
- Moritz, R. E., and D. K. Perovich, Eds., *SHEBA, A Research Program on the Surface Heat Budget of the Arctic Ocean, Science Plan*, Rep. No. 5, U. of Washington, 64 pp., 1996.
- Neumann G., and W. J. Pierson, Jr., *Principles of Physical Oceanography*, Prentice-Hall, Inc., Englewood Cliffs, N. J., 1966.
- Nghiem, S. V., R. Kwok, S. H. Yueh, and M. R. Drinkwater, Polarimetric signatures of sea ice, 1, Theoretical model, *J. Geophys. Res.*, *100*(C7), 13665-13679, 1995a.
- Nghiem, S. V., R. Kwok, S. H. Yueh, and M. R. Drinkwater, Polarimetric signatures of

- sea ice, 2, Experimental observations, *J. Geophys. Res.*, 100(C7), 13681-13698, 1995b.
- Nghiem, S. V., R. Kwok, S. H. Yueh, A. J. Gow, D. K. Perovich, J. A. Kong, and C. C. Hsu, Evolution in polarimetric signatures of thin saline ice under constant growth, *Radio Sci.*, 32(1), 127-151, 1997a.
- Nghiem, S. V., S. Martin, D. K. Perovich, R. Kwok, R. Drucker, and A. J. Gow, A laboratory study of the effects of frost flowers on C-band radar backscatter from sea ice, *J. Geophys. Res.*, 102(C2), 3357-3370, 1997b.
- Nghiem, S. V., R. Kwok, S. H. Yueh, D. K. Perovich, A. J. Gow, C. C. Hsu, K. H. Ding, J. A. Kong, and T. C. Grenfell, Diurnal thermal cycling effects on backscatter of thin sea ice, *IEEE Trans. Geosci. Remote Sens.*, 36(1), 111-124, 1998a.
- S. V. Nghiem, Sea ice surface thermal states in polar regions, in *Arctic Ocean Science from Submarines – A Report based on the SCICEX 2000 Workshop*, D. Rothrock, W. Maslowski, D. Chayes, G. Flato, J. Grebmeier, R. Jackson, R. Sambrotto, W. Smethie, W. Sternberger, J. Swift, J. Tarduno, and A. Thorndike, Section F, pp. 31-32, Univ. Washington, Seattle, WA, 1999.
- Olmsted, Alaska SAR facility scientific SAR user's guide, *Tech. Rep. ASF-SD-003*, Alaska SAR Facility, Geophys. Inst., Univ. Alaska, Fairbanks, 1993.
- Onstott, R. G., SAR and scatterometer signatures of sea ice, *Geophysical Monograph Ser.*, 68, F. D. Carsey ed., 73-104, 1992.
- Perovich D. K., and A. J. Gow, A statistical description of microstructure of young ice, *J. Geophys. Res.*, 96(C9), 16943-16953, 1991.
- Perovich, D. K., and others, Year on ice gives climate insights, *EOS, Trans.*, Amer. Geophys. Union, 80(481), 485-486, 1999a.
- Perovich, D. K., T. C. Grenfell, B. Light, J. A. Richter-Menge, M. Sturm, W. B. Tucker III, H. Eicken, G. A. Maykut, B. Elder, *SHEBA: Snow and Ice Studies CD-ROM*,

October, 1999b.

- Rind, D., R. Healy, C. Parkinson, and D. Martinson, The role of sea ice in $2 \times \text{CO}_2$ climate model sensitivity, I: The total influence of total sea ice thickness and extent, *J. Climate*, 8, 449-463, 1995.
- Simpson, J. J. and S. R. Yhann, Reduction of noise in AVHRR channel 3 data with minimum distortion, *IEEE Trans. Geosci. Remote Sens.*, 32(2), 315-328, 1994.
- Swift, C. T., K. St. Germain, K. C. Jezek, S. P. Gogineni, A. J. Gow, D. K. Perovich, T. C. Grenfell, and R. G. Onstott, Laboratory investigations of the electromagnetic properties of artificial sea ice, *Geophysical Monograph Ser.*, 68, F. D. Carsey ed., 177-200, 1992.
- U. S. Army TECOM Hanover Meteorological Team, Monthly meteorological data, CRREL test cell, *Intern. Rep.*, Atmos. Sci. Div., U. S. Army Corps of Engineers, Cold Regions Research and Engineering Laboratory, Hanover, N. H., 1995.
- Weeks, W. F., and S. F. Ackley, *The Growth, Structure, and Properties of Sea Ice*, *Monogr. Ser.*, 82-1, U. S. Army Corps of Engineers, Cold Regions Research and Engineering Laboratory, Hanover, N. H., 1982.
- Yamanouchi, T., K. Suzuki, S. Wawaguchi, Detection of clouds in Antarctica from infrared multispectral data of AVHRR, *J. Met. Soc. of Japan*, 65(6), 949-961, 1987.

LIST OF FIGURES

- Figure 1.** Top view of the experimental setup at the Geophysical Research Facility at CRREL. The JPL scatterometer was mounted on the movable gantry about 4 m above the sea ice sheet.
- Figure 2.** Photo of the scatterometer on the gantry. The diagonal horn is the antenna and the insulated box contains radio-frequency electronic components. A video camera wrapped in a heating pad is installed under the frame beneath the antenna. A partly cloudy sky condition is seen in the background.
- Figure 3.** Atmospheric conditions measured by the CRREL Meteorological Station: (a) the top left panel shows downward incoming short-wave radiation, (b) the top right panel is for downward long-wave radiation, (c) the bottom left panel presents wind speed, and (d) the bottom right panel reports air temperature during the experimental period from 6:00 am on 19 February to 6:00 am on 20 February 1995.
- Figure 4.** Temperatures over sea ice: (a) the left panel plots of temperatures T_{3cm} and T_{8cm} measured with a thermistor string at 3 cm and 8 cm above the ice surface, and (b) the right panel plots temperature T_{sur} within 1 cm above the ice surface and temperature T_{air} measured with a digital thermometer at 1.2 m above the ice surface. Temperature T_{fit} represented by a dotted curve in the right panel is a polynomial fit of T_{sur} .
- Figure 5.** Salinity profile for the 34-cm thick sea ice sheet. Note the high salinity in the top layer of the ice sheet.
- Figure 6.** Temperature and brine profiles in the sea ice sheet. The vertical axis is depth

in cm: above 0 cm is air denoted by the light blue color, below 34 cm is sea water represented by the dark blue color, and in between is sea ice where the color change from red to yellow corresponds to brine volume fraction change from 2% to 35%. The continuous curves are for temperatures plotted over the horizontal axis ranged from -10°C to 10°C .

- Figure 7.** Brine channels observed in situ at 09:45 am on 20 February 1995.
- Figure 8.** Vertical and horizontal thin section photographs showing the structural characteristics and brine inclusion features in the sea ice sheet.
- Figure 9.** Backscatter σ_{hh} (represented by squares) and σ_{vv} (represented by triangles) at 20° , 25° , 30° , and 35° incident angles. The background color from dark blue (-8°C) to bright yellow (-2°C) corresponds to temperature T_{fit} near the ice surface at the given time.
- Figure 10.** Backscatter copolarized ratio γ , crosspolarized ratio e , magnitude of ρ , and phase of ρ at 20° , 25° , 30° , and 35° incident angles. The background color represents the near ice surface temperature with the same scale in Figure 9.
- Figure 11.** Comparison of backscatter change in response to ice surface temperature change for (a) horizontal and (b) vertical polarizations. The light-grey bars are for 1995 data and the dark-grey bars are for 1994 data.
- Figure 12.** Brine volume in sea ice versus temperature. The curves from the lowest to the highest are for salinities from 4 ‰ to 16 ‰ for every 2 ‰ increment. Triangles, squares, and circles are for crystallization points of $\text{CaCO}_3 \cdot 6\text{H}_2\text{O}$, $\text{Na}_2\text{SO}_4 \cdot 10\text{H}_2\text{O}$ (mirabilite), and $\text{MgCl}_2 \cdot 8\text{H}_2\text{O}$, respectively.
- Figure 13.** Temperature images from AVHRR Channel 4: (a) 6 May 1993 under a clear

sky, and (b) 9 May 1993 under cloud cover. G marks Griffith Island and C marks Cornwallis Island.

Figure 14. Albedo images from AVHRR Channel 1: (a) 6 May 1993 under a clear sky, and (b) 9 May 1993 under cloud cover. G marks Griffith Island and C marks Cornwallis Island.

Figure 15. ERS-1 SAR results: (a) SAR image of the C-ICE area with field experiment data for ice and snow thicknesses over different consolidation periods, and (b) Processed image of backscatter increase obtained by taking the difference of backscatter between 9 May 1993 under cloud cover and 6 May 1993 under a clear sky. G marks Griffith Island and C marks Cornwallis Island. The result in this figure is adapted after Baber and Nghiem [1999].

LIST OF TABLES

Table 1. Correlation between backscatter and temperature T_{sur} near the ice surface during the cooling cycle for (a) horizontal polarization and (b) vertical polarization. Parameter α is the change in backscatter corresponding to 1°C change in temperature, β is the linear-fit backscatter at 0°C , δ is the standard deviation, and ρ_c is the correlation coefficient between backscatter and temperature.

Table 2. Correlation between backscatter and air temperature T_{air} during the cooling cycle for (a) horizontal polarization and (b) vertical polarization. Parameter α is the change in backscatter corresponding to 1°C change in temperature, β is the linear-fit backscatter at 0°C , δ is the standard deviation, and ρ_c is the correlation coefficient between backscatter and temperature.

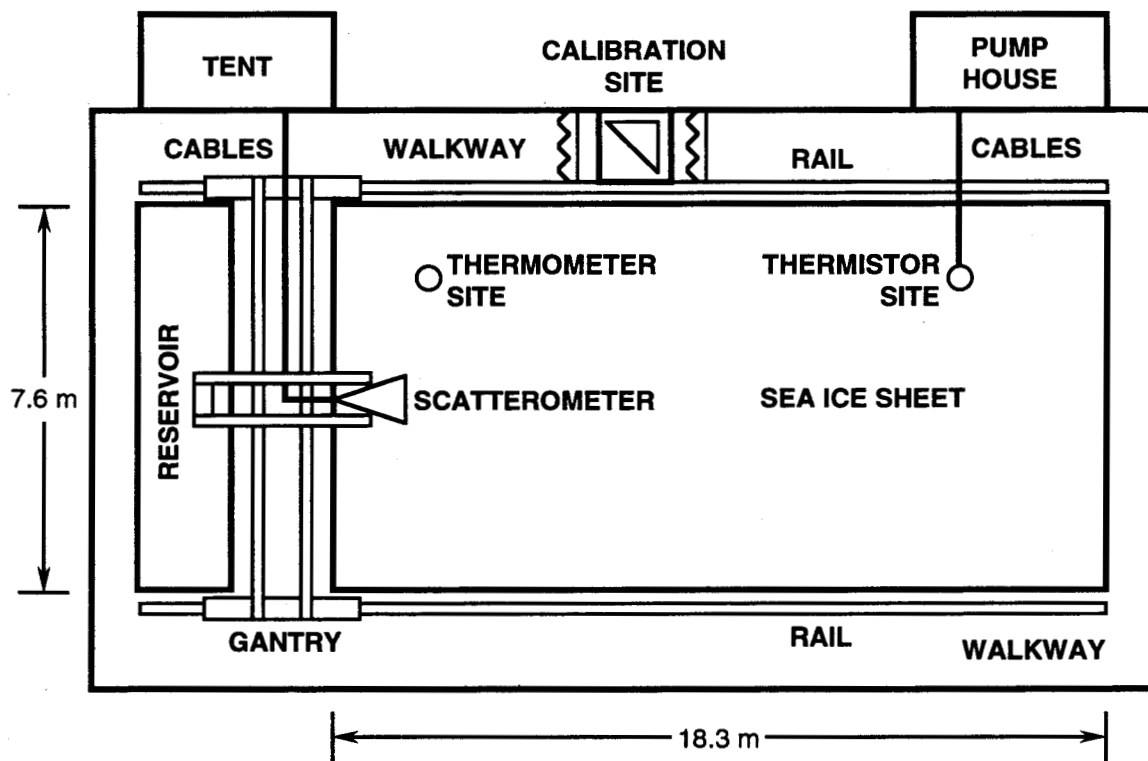
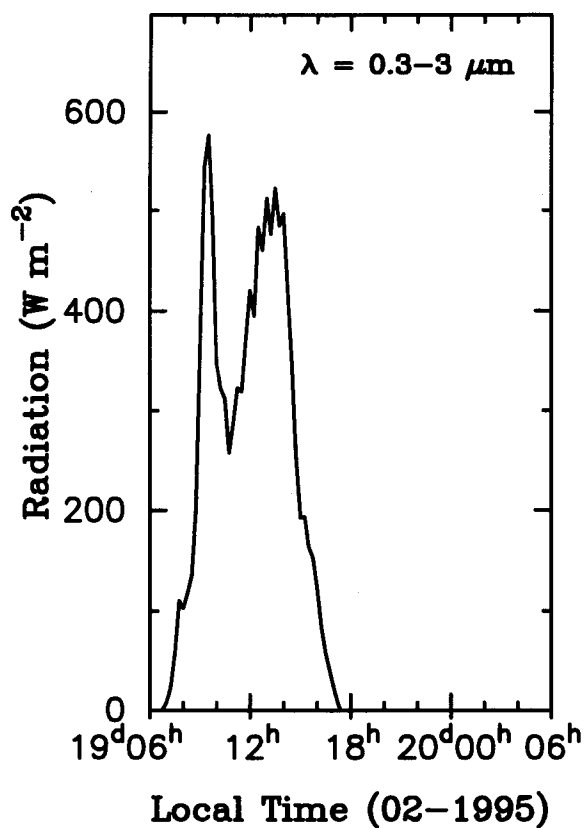


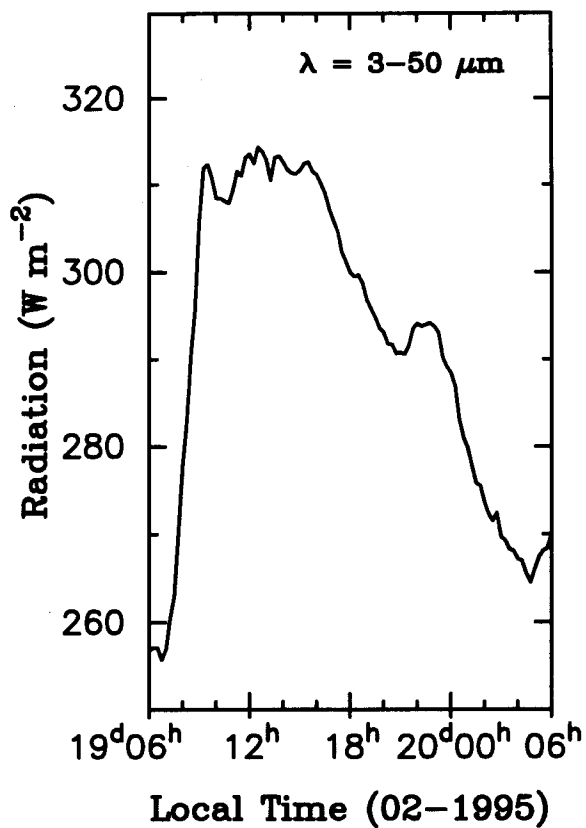
Figure 1



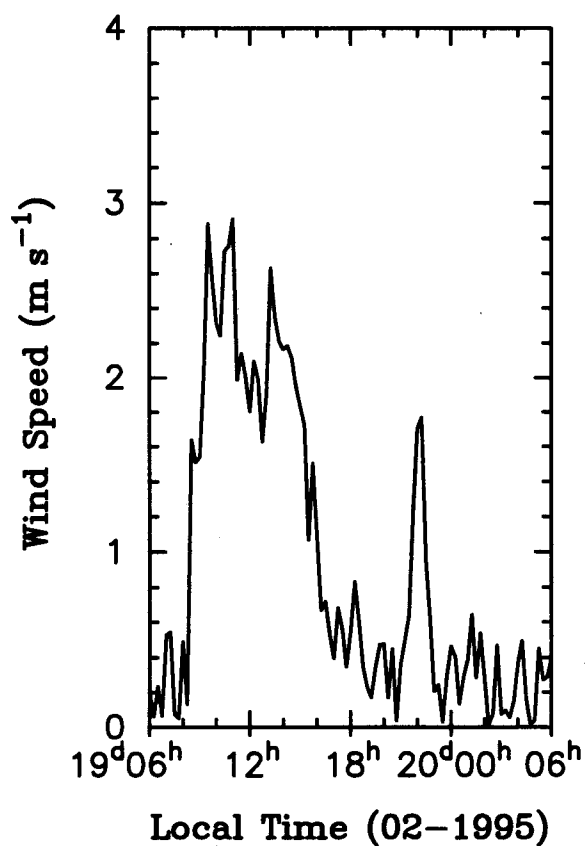
Short Waves



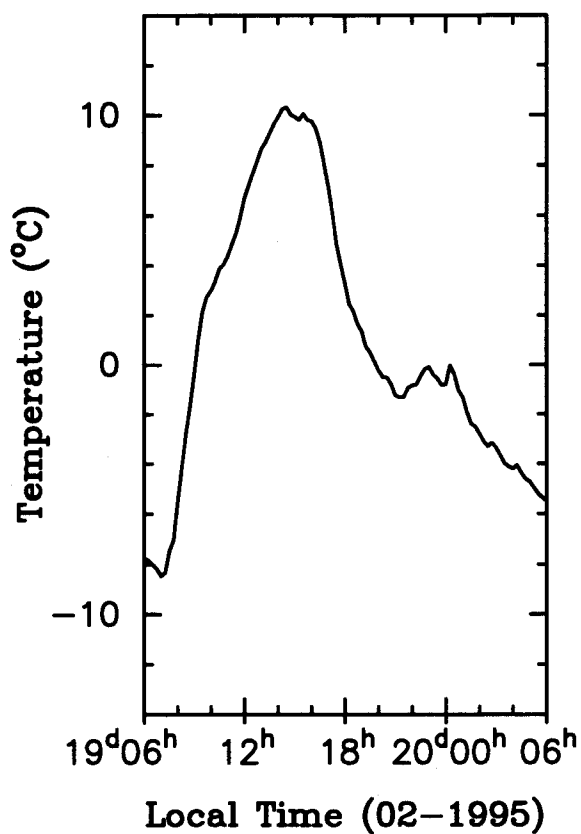
Long Waves



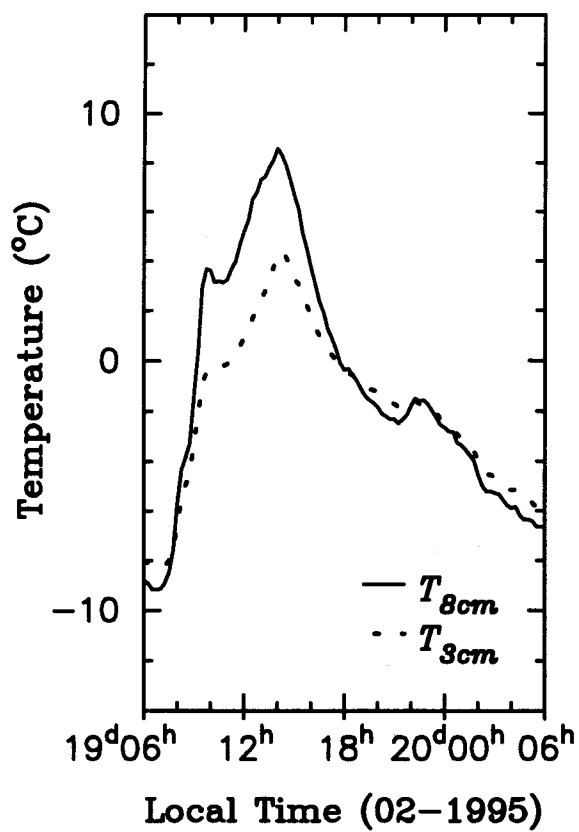
Wind Speed



Air Temperature



Thermistor



Thermometer

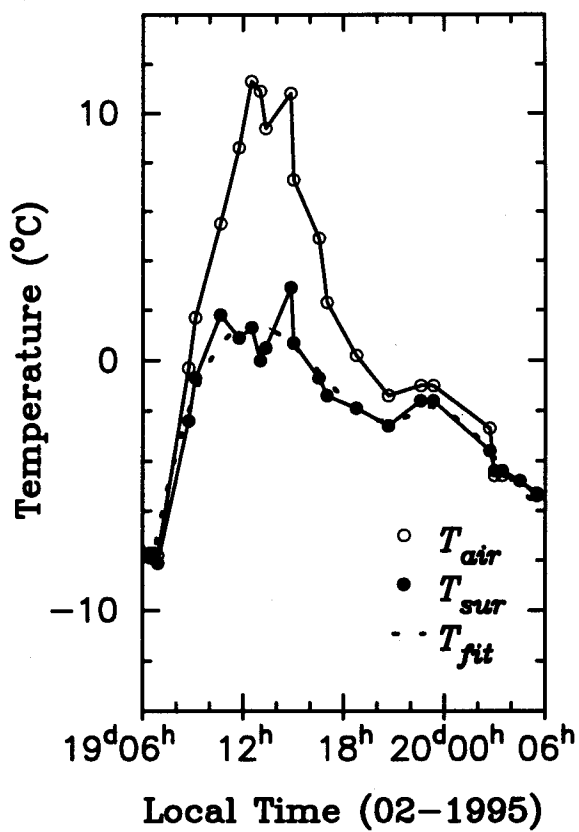
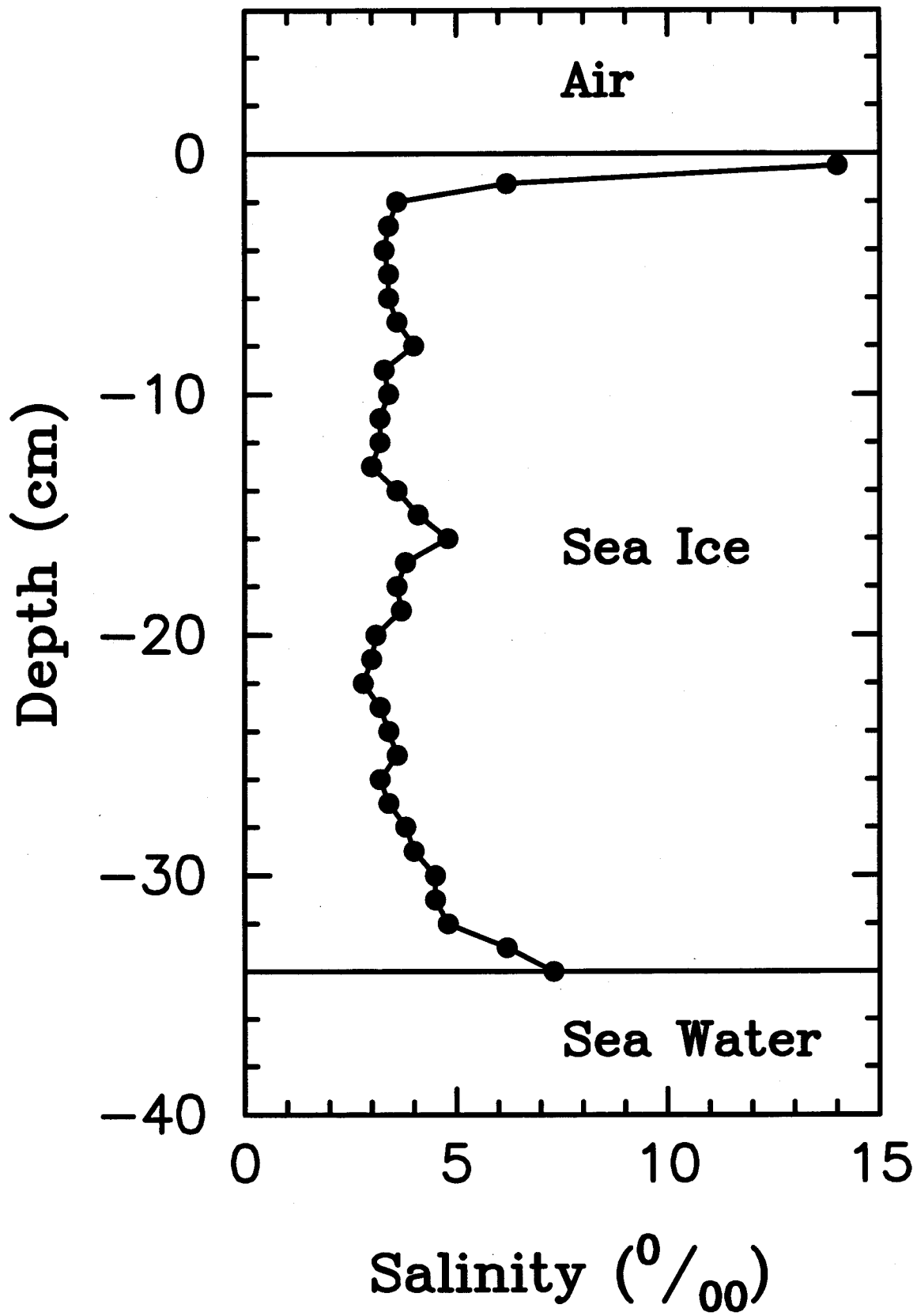


FIG.5



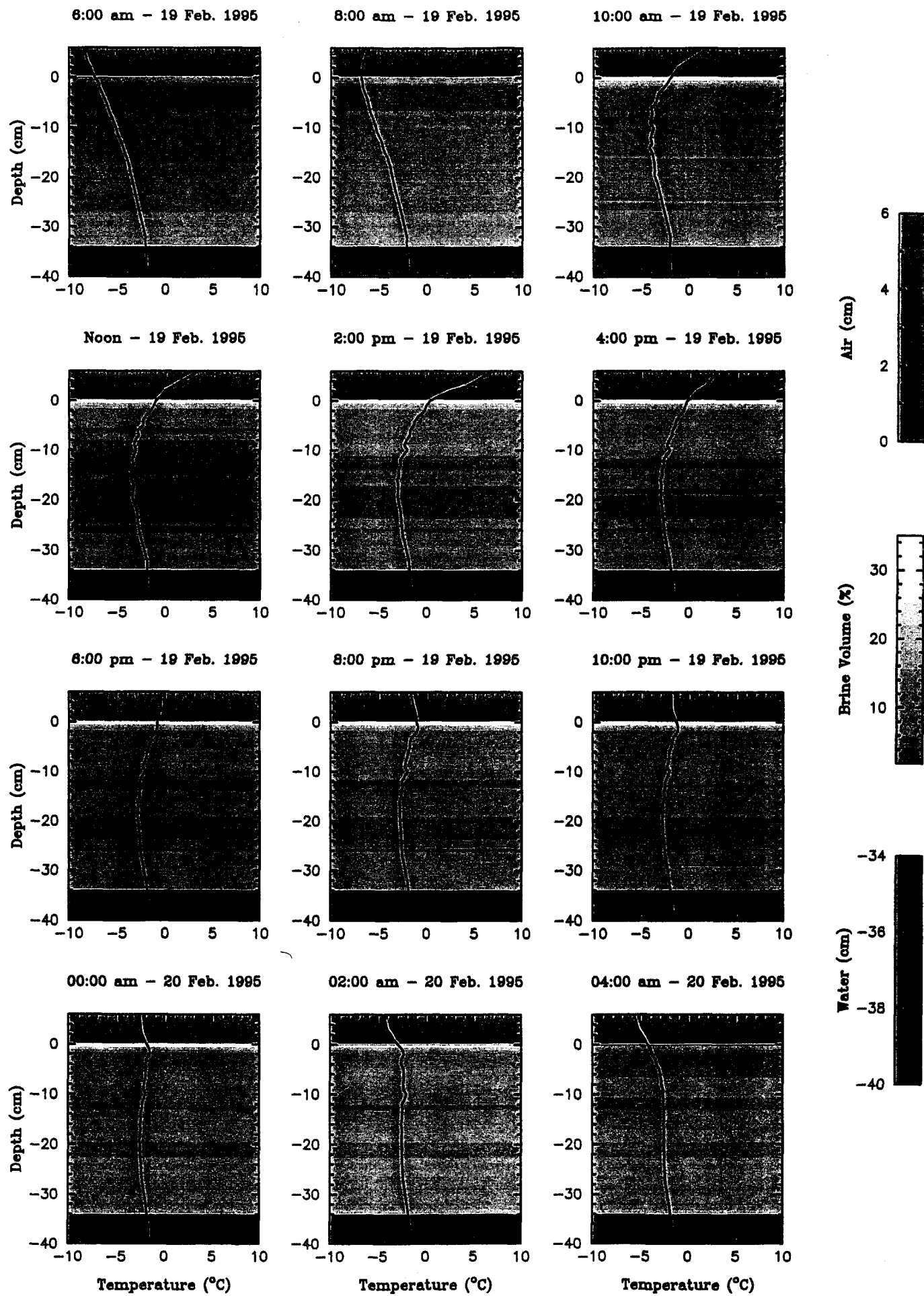
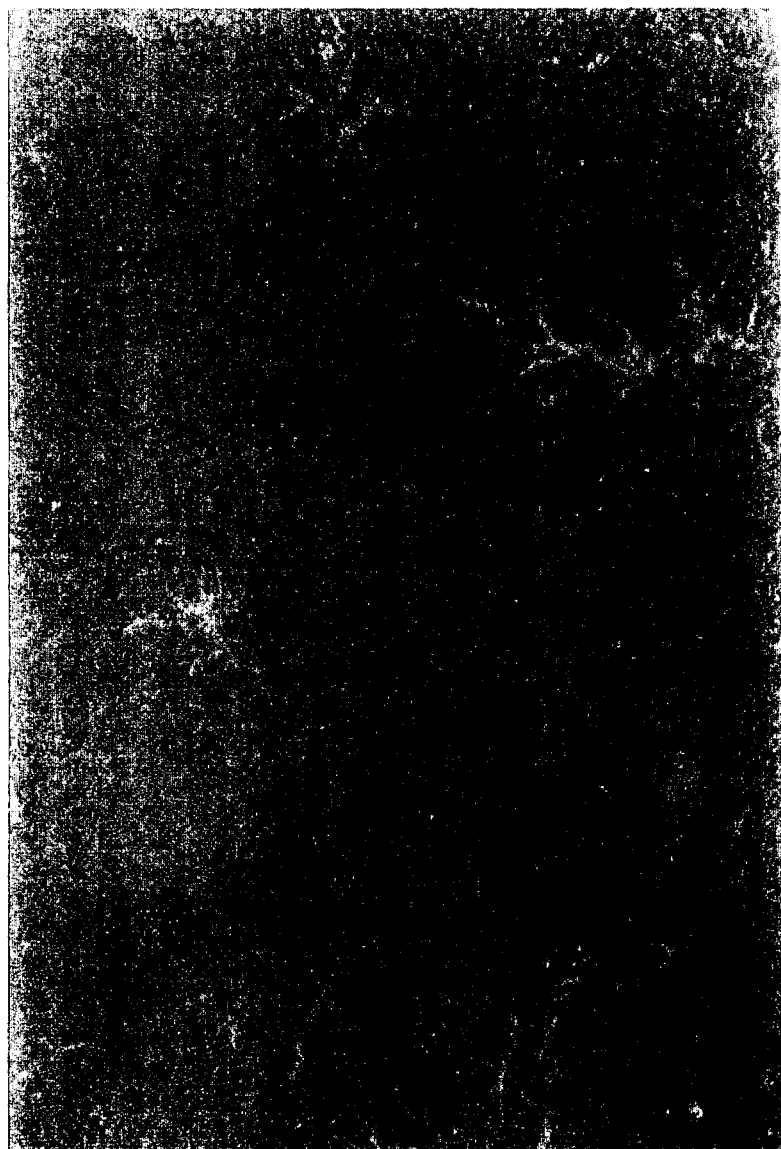


Fig. 1



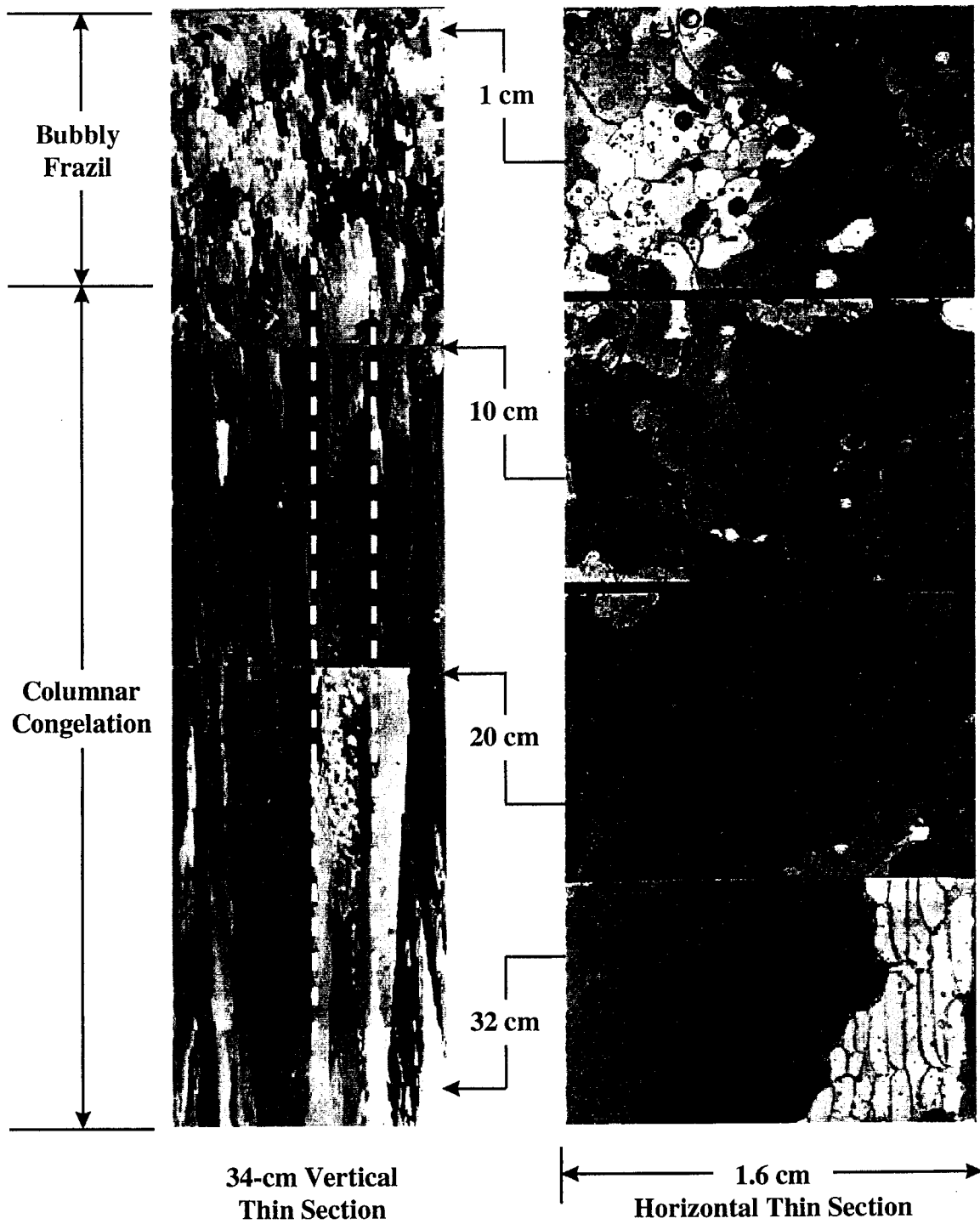
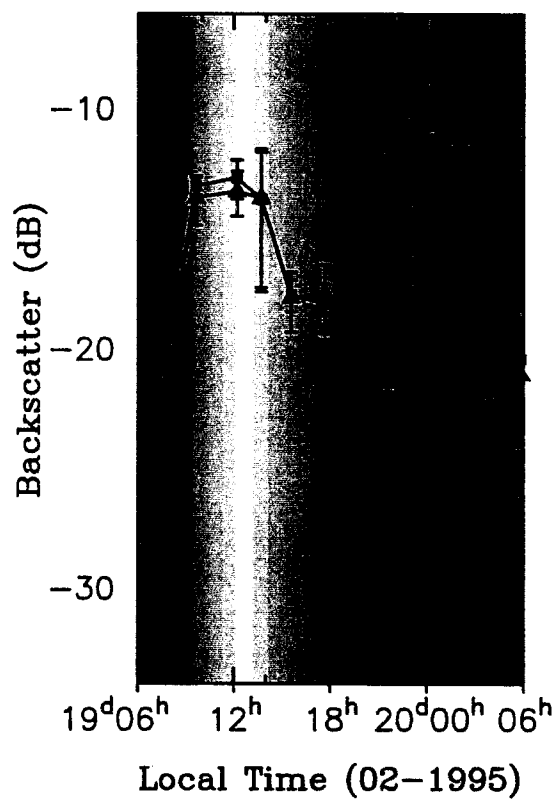
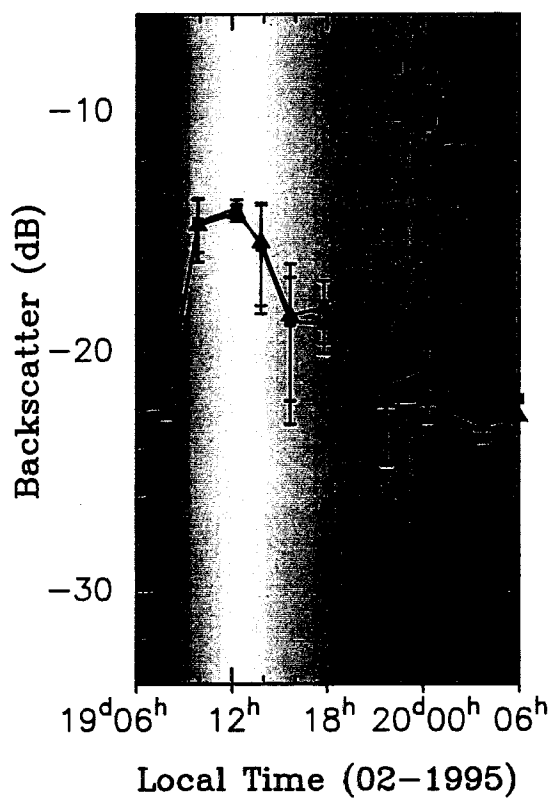


Figure 8

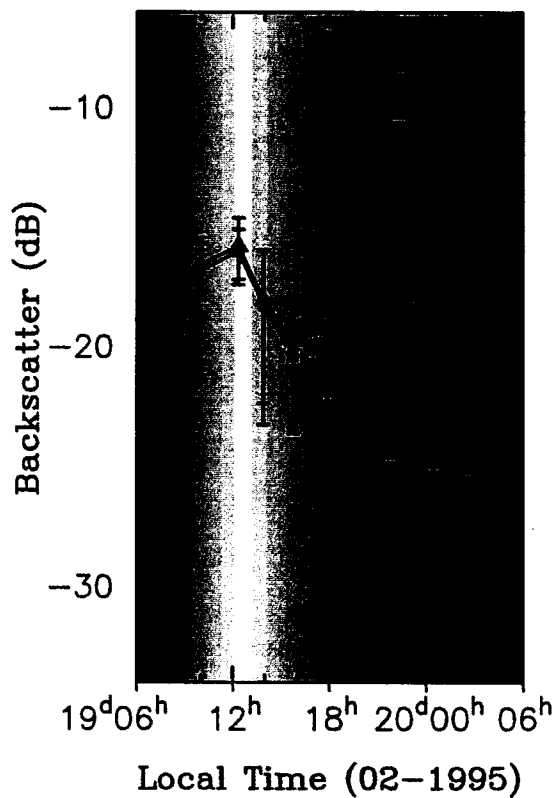
20° Incident Angle



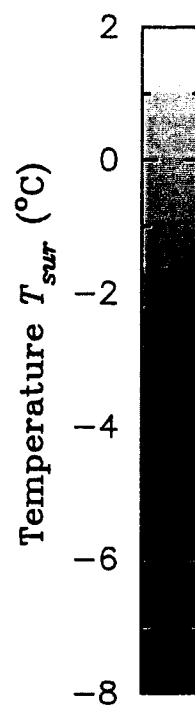
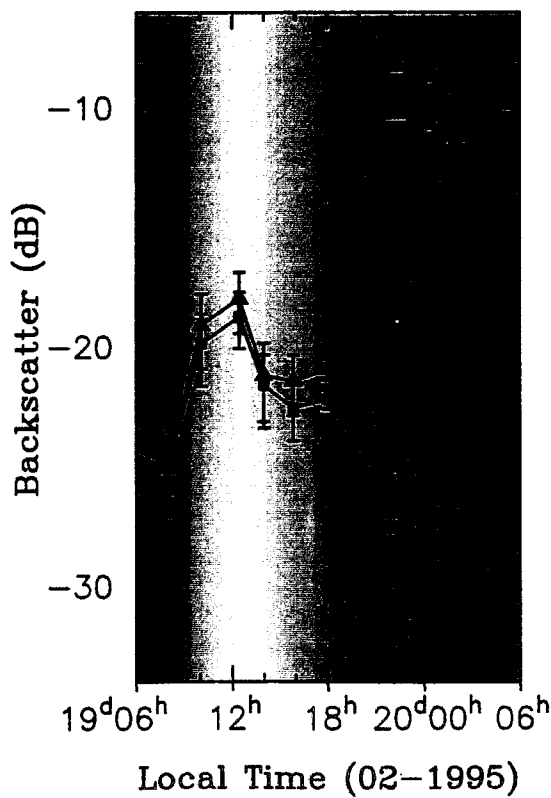
25° Incident Angle

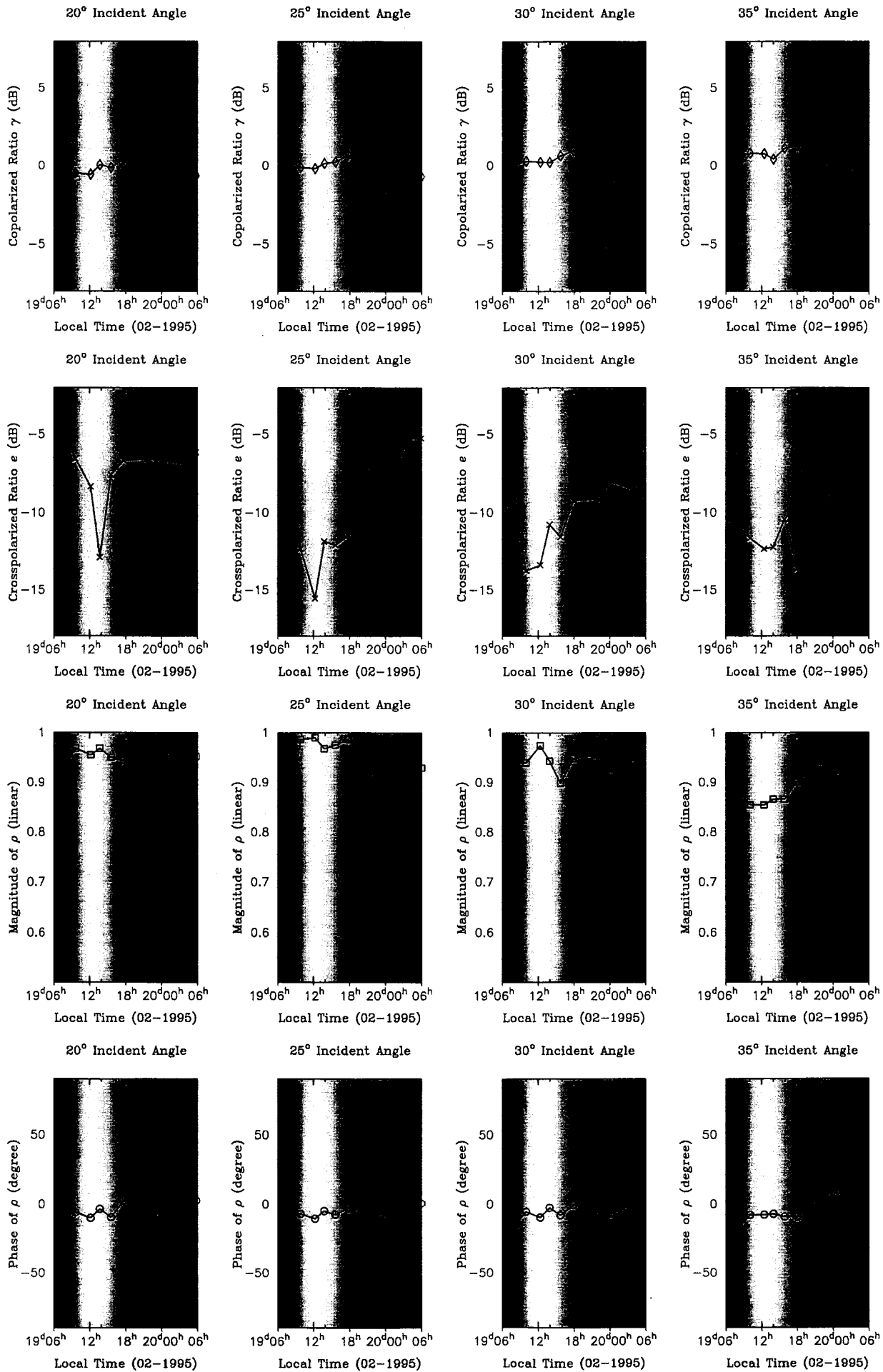


30° Incident Angle

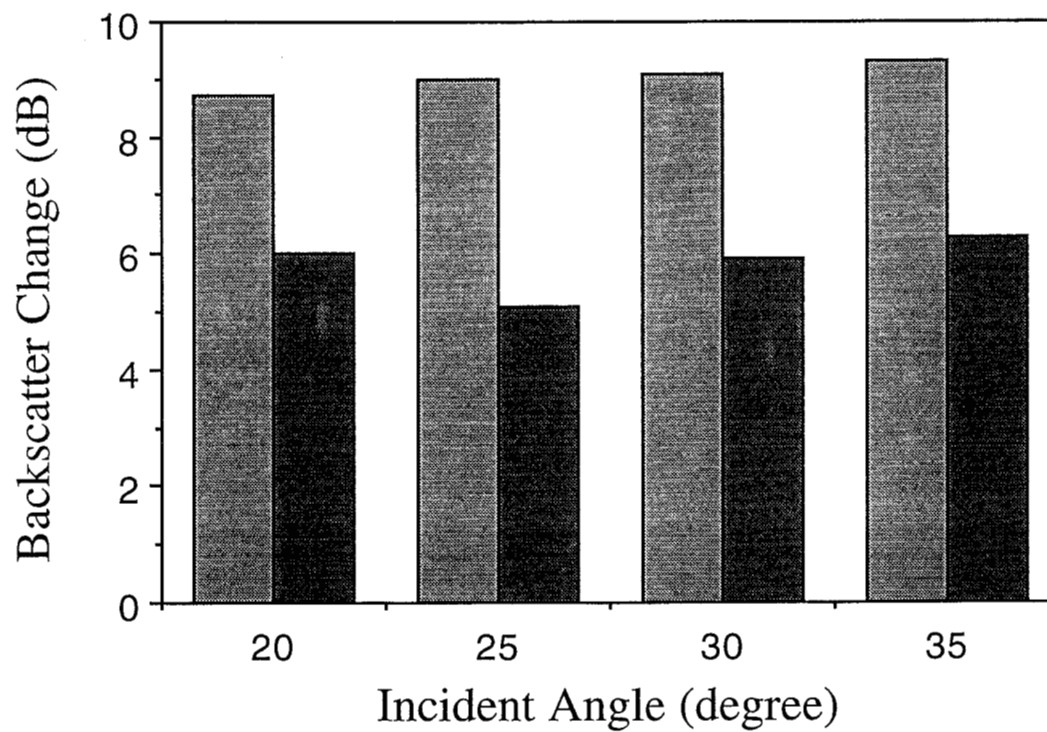


35° Incident Angle





(a) Horizontal Polarization



(b) Vertical Polarization

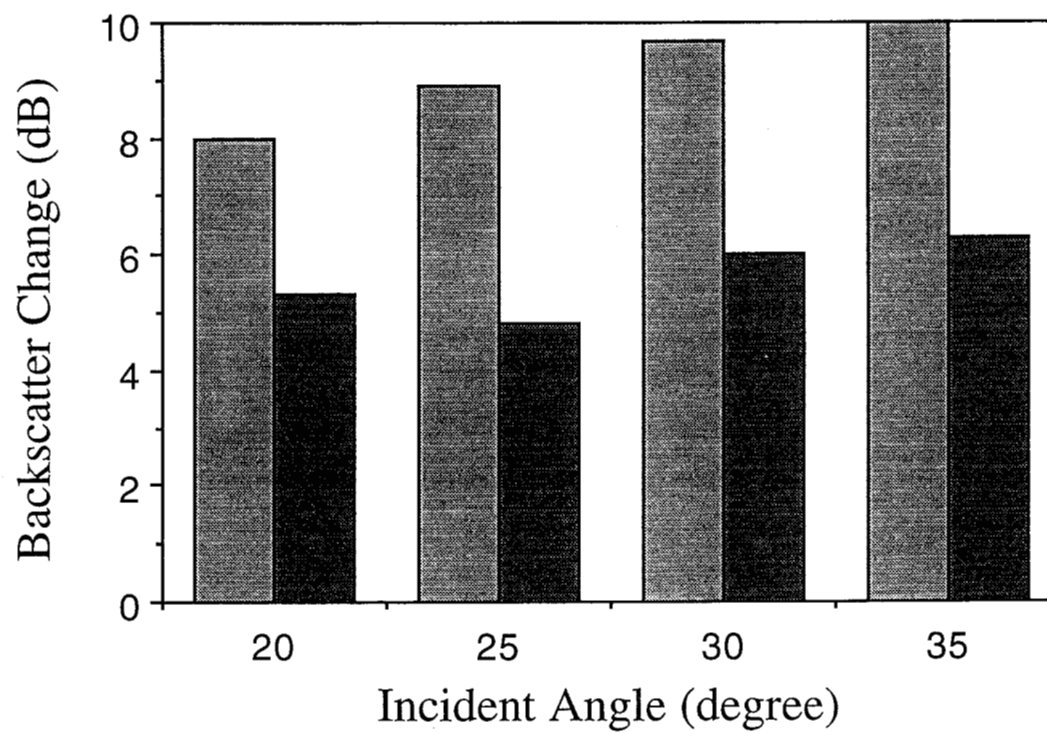
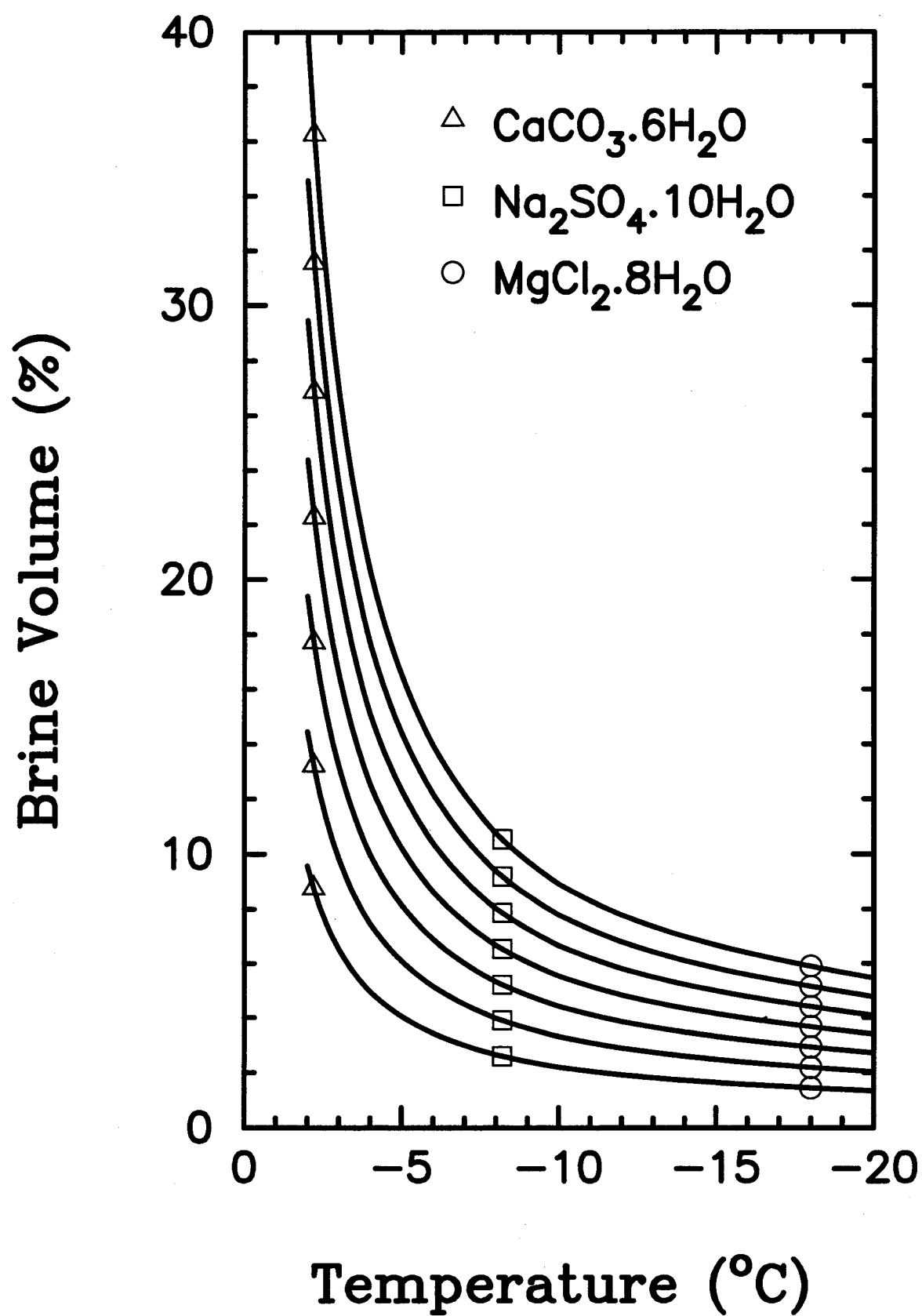


FIG. 12



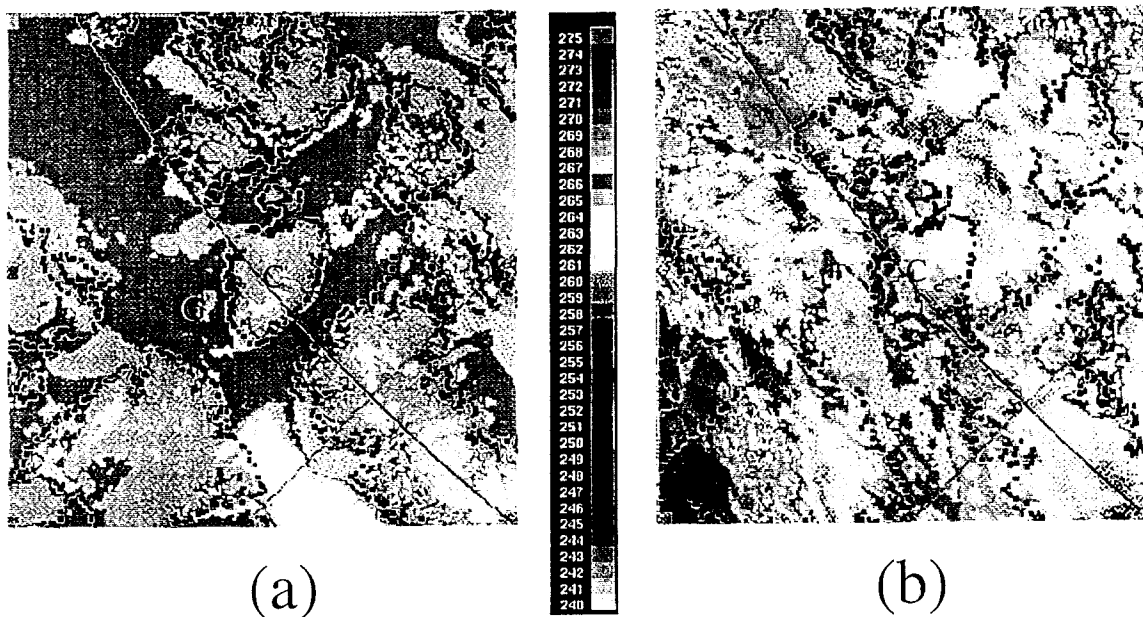


Figure 13: Temperature images from AVHRR Channel 4: (a) 6 May 1993 under a clear sky and (b) 9 May 1993 under cloud cover. G is for Griffith Island and C for Cornwallis Island

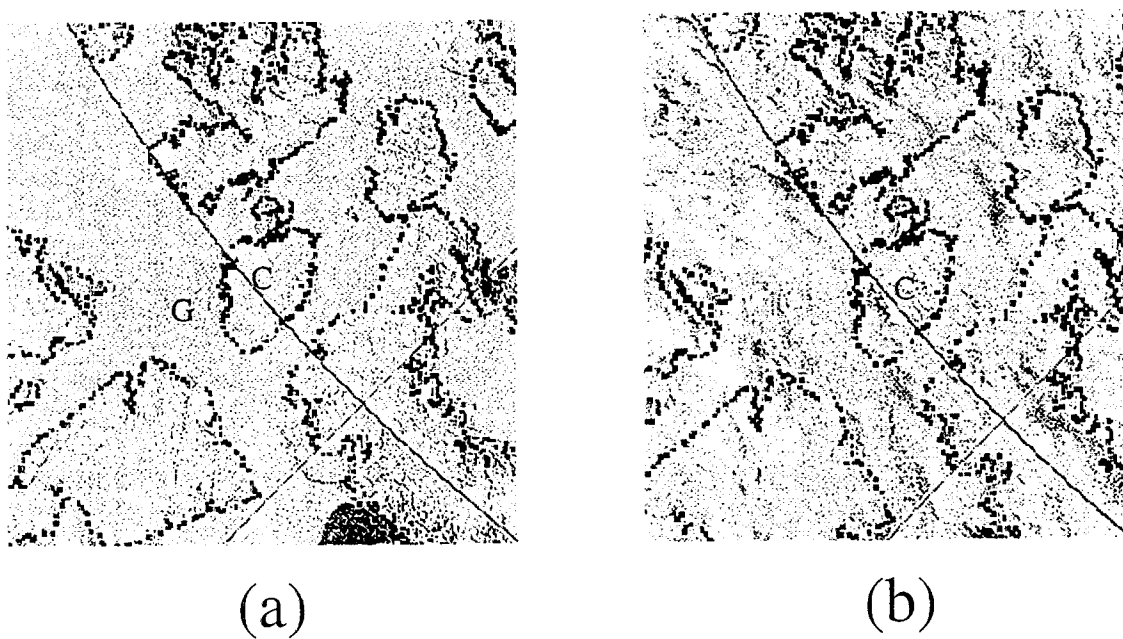


Figure 14: Albedo images from AVHRR Channel 1: (a) 6 May 1993 under a clear sky and (b) 9 May 1993 under cloud cover. G is for Griffith Island and C for Cornwallis Island

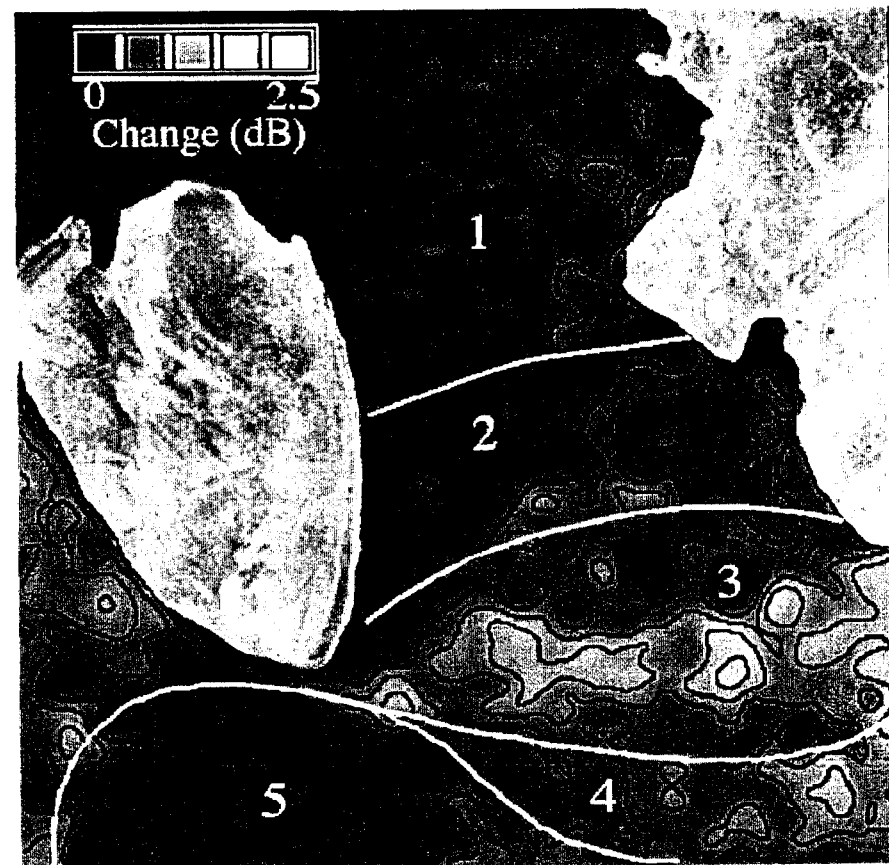
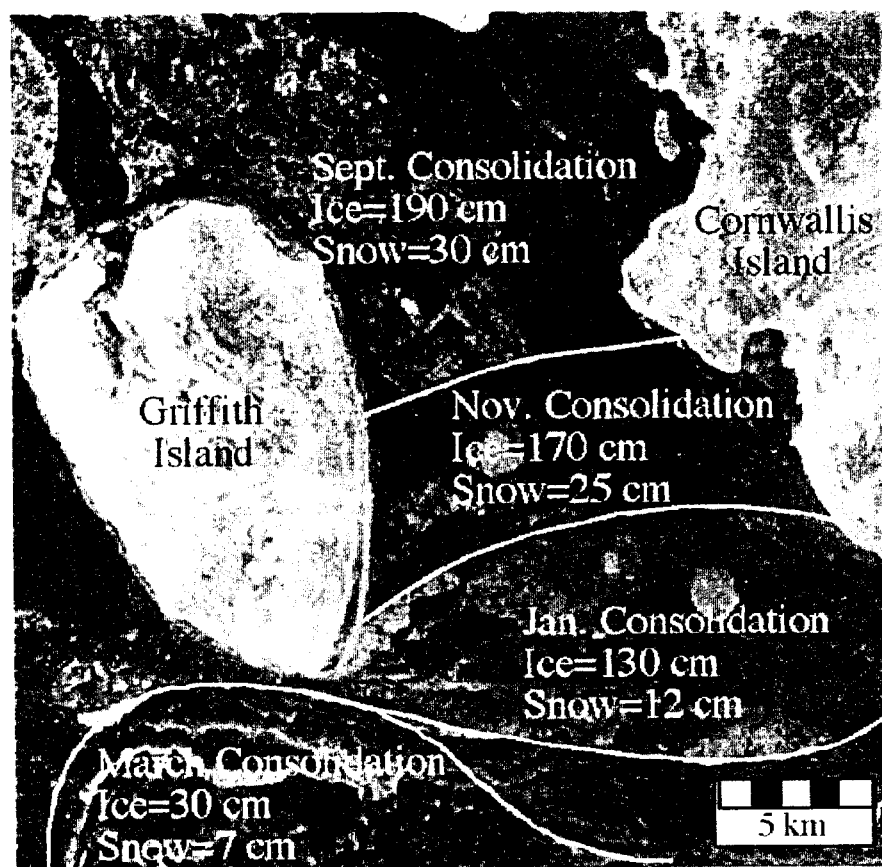


FIG. 15

(a) Horizontal backscatter σ_{hh} :

θ	α (dB/°C)	β (dB)	δ (dB)	ρ_c
20°	1.1	-16.2	1.5	0.84
25°	1.1	-17.6	1.5	0.86
30°	1.2	-19.3	1.5	0.85
35°	1.1	-22.2	2.0	0.76

(b) Vertical backscatter σ_{vv} :

θ	α (dB/°C)	β (dB)	δ (dB)	ρ_c
20°	1.1	-16.6	1.7	0.82
25°	1.2	-17.8	1.7	0.84
30°	1.3	-19.1	1.9	0.83
35°	1.3	-21.4	2.1	0.80

Table 1. Correlation between backscatter and temperature T_{sur} near the ice surface during the cooling cycle for (a) horizontal polarization and (b) vertical polarization. Parameter α is the change in backscatter corresponding to 1°C change in temperature, β is the linear-fit backscatter at 0°C, δ is the standard deviation, and ρ_c is the correlation coefficient between backscatter and temperature.

(a) Horizontal backscatter σ_{hh} :

θ	α (dB/°C)	β (dB)	δ (dB)	ρ_c
20°	0.45	-18.8	1.0	0.93
25°	0.47	-20.4	0.8	0.96
30°	0.50	-22.3	0.9	0.95
35°	0.48	-25.0	1.5	0.88

(b) Vertical backscatter σ_{vv} :

θ	α (dB/°C)	β (dB)	δ (dB)	ρ_c
20°	0.48	-19.3	0.9	0.94
25°	0.52	-20.8	0.9	0.96
30°	0.55	-22.4	1.3	0.92
35°	0.54	-24.7	1.6	0.88

Table 2. Correlation between backscatter and air temperature T_{air} during the cooling cycle for (a) horizontal polarization and (b) vertical polarization. Parameter α is the change in backscatter corresponding to 1°C change in temperature, β is the linear-fit backscatter at 0°C, δ is the standard deviation, and ρ_c is the correlation coefficient between backscatter and temperature.